PHYSICAL PROPERTIES OF Pd, Ni METALS AND THEIR BINARY ALLOYS

A THESIS SUBMITTED TO
THE GRADUATE SCHOOL OF NATURAL AND APPLIED SCIENCES
OF
THE MIDDLE EAST TECHNICAL UNIVERSITY

BY

SEVGİ ÖZDEMİR KART

IN PARTIAL FULFILLMENT OF THE REQUIREMENTS FOR THE DEGREE OF

DOCTOR OF PHILOSOPHY

IN

THE DEPARTMENT OF PHYSICS

APRIL 2004

Approval of the Graduate School of Natural and Applied Sciences.

Prof. Dr. Canan Özgen
Director

I certify that this thesis satisfies all the requirements as a thesis for the degree of Doctor of Philosophy.

Prof. Dr. Sinan Bilikmen
Head of Department

This is to certify that we have read this thesis and that in our opinion it is fully adequate, in scope and quality, as a thesis for the degree of Doctor of Philosophy.

Prof. Dr. Mehmet Tomak
Supervisor

Examining Committee Members

Prof. Dr. Bülent Karasözen

Prof. Dr. Cevdet Tezcan

Prof. Dr. Mehmet Tomak

Assoc. Prof. Dr. Hatice Kökten

Dr. Sadi Turgut

ABSTRACT

PHYSICAL PROPERTIES OF Pd, Ni METALS AND THEIR BINARY ALLOYS

Özdemir Kart, Sevgi

Ph. D., Department of Physics

Supervisor: Prof. Dr. Mehmet Tomak

April 2004, 88 pages.

The Sutton Chen and quantum Sutton Chen potentials are used in molecular dynamics simulations to describe the structural, thermodynamical, and transport properties of Pd, Ni and their binary alloys in solid, liquid, and glass phases. Static properties including elastic constants, pair distribution function, static structure factor, and dynamical properties consisting of phonon dispersion relation, diffusion coefficient, and viscosity are computed at various temperatures. The melting temperatures for Pd-Ni system are obtained. The transferability of the potentials is tested by simulating the solid and liquid states. The eutectic concentration $Pd_{0.45}Ni_{0.55}$ is quenched at four different cooling rates. The system goes into glass formation at fast cooling rates, while it evolves to crystal at slow cooling rate. Comparison of calculated structural and dynamical properties with the available experiments and other calculations shows satisfactory consistency.

Keywords: Molecular Dynamics Simulation, Metals and Metal Alloys, Liquid Metals, Phonon Dispersion Relation, Elastic Constant, Diffusion Coefficient, Viscosity, Melting Temperature, Metallic Glass.

ÖZ

Pd, Ni METALLERİ VE İKİLİ ALAŞIMLARININ FİZİKSEL ÖZELLİKLERİ

Özdemir Kart, Sevgi
Doktora, Fizik Bölümü
Tez Yöneticisi: Prof. Dr. Mehmet Tomak

Nisan 2004, 88 sayfa.

Pd, Ni ve ikili alaşımlarının katı, sıvı ve camsı fazlarda yapısal, termodinamiksel ve transport özelliklerini açıklamak için Sutton-Chen ve quantum Sutton-Chen potansiyelleri moleküler dinamik simülasyonlarında kullanıldı. Elastik sabiti, çift dağılım fonksiyonu ve statik yapı faktörü statik özellikler olarak, ve fonon dispersiyon ilişkisi, difüzyon katsayısı ve viskosite içeren dinamik özellikler değişik sıcaklıklarda hesaplandı. Pd-Ni sisteminin erime sıcaklıkları elde edildi. Sistemin katı ve sıvı fazı simüle ederek potansiyelin uyarlanabilirliği test edildi. $Pd_{0.45}Ni_{0.55}$ alaşımı dört farklı soğutma hızında soğutulmuştur. Sistem yüksek soğutma hızlarında camsı yapıya dönüşürken, yavaş soğutma hızında kristalleşir. Hesaplanan statik ve dinamik özellikler mevcut deneysel ve diğer simülasyon çalışmalarıyla karşılaştırılması sonucu yeterli derecede uyumlu oldukları görülmüştür.

Anahtar Kelimeler: Moleküler Dinamik Simülasyonu, Metaller ve Metal Alaşımları, Sıvı Metaller, Fonon Dispersiyon İlişkisi, Elastik Sabiti, Difüzyon Katsayısı, Viskosite, Erime Sıcaklığı, Camsı Metaller.

ACKNOWLEDGMENTS

I would like to express my deep gratitude and thanks to Prof. Dr. Mehmet Tomak for his excellent supervision, encouragement, continuous support, and invaluable guidance, for the trust and freedom he gave me during this work.

I would like to thank Dr. Tahir Çağın for providing molecular dynamics simulation program. I am grateful to Dr. Mustafa Uludoğan for making me be familiar with the simulation program.

My special thanks also go to Assoc. Prof. Dr. Hatice Kökten for being a mentor and a friend, as well as helping me overcome the hard times with her crucial advices on life. I also thank my best friend Sema Memiş for her encouragement and friendship.

Lastly, I dedicate this dissertation to my parents, my husband and my daughter, Ahsen Gül whose love and being give me more exciting life than I can imagine. I would like to express my gratitude and my appreciation to my husband, Hasan Hüseyin, for his love, support, encouragement, helping me write this thesis, and giving me a happy and complete life. I am very much indebted to my family for their continuous support and their love. Particularly, my special thanks to my mother for looking after my baby during this study.

... To My Parents, My Husband

&

My Daughter Ahsen Gül

TABLE OF CONTENTS

LIST OF TABLES

CHAPTER 1

INTRODUCTION

Recent advances in numerical methods and computer technology have reinforced attempts to study the physical properties of metal alloys. A detailed research on the development of materials is of great interest for their industrial applications. Palladium and its alloys have industrial importance because of their hardness and resistance to corrosion.

The knowledge of structural, thermodynamic, and atomic transport properties of liquid Pd-Ni alloys play important roles in the industrial applications. It is used in hydrogen sensors. The understanding of their physical properties remains a challenge. This alloy has also glass forming properties at the eutectic region around 45 % of Pd. Thus the knowledge of the liquid properties of Pd-Ni alloys is required for investigating the solidification process. Hence, it is important to investigate the physical properties of Pd-Ni alloys in solid, liquid, and glass phases. In this work we aim to simulate Pd-Ni alloys.

The study of the lattice-dynamical properties of metals and their alloys remains as one of the most interesting topics, both theoretically and experimentally. The easiest test of dynamical properties is the calculation of phonon dispersion curves, for which experimental measurements are available. In particular, the

knowledge of the phonon spectrum is an essential input to the calculation of heat capacities, thermal expansion coefficients, electron-phonon interactions, etc.

Calculations of the phonon spectra for fcc transition metals have been carried out in the past mostly using two-body potentials. Singh *et al.* [1] described the phonon properties for some transition metals including Pd and Ni. Barrera and Batana studied lattice dynamics of noble metals (Cu, Ag, Au) [2] and semi-noble metals (Pd, Ni, Pt) [3] by using two and three-body potentials. Recently, in a work by Singh [4], structural phase transformations of Cu, Pd and Au using transition metal pair potential (TMPP) [5] was studied and it was stated that one should consider many-body potentials instead of two-body potentials to reproduce all properties of the transition metals including bulk modulus. Brovman and Kagan [6] realized the importance of many-body forces in the lattice dynamics of metals and showed that the terms higher than the second order in perturbation expansion are necessary for the equality of the values of compressibility calculated by long waves method and the method of homogeneous deformations. This indicates that many-body potentials are essential to account for long wavelength phonons.

Pd-Ni system forms a random disordered alloy with high-concentration mass at the eutectic region and it is convenient for an experiment by inelastic neutron scattering [7]. Due to availablity of experimental data, it has been investigated by several workers [8, 9]. They used the transition metal model potential (TMMP) of Animalu [10] to obtain phonon dispersion curves of $Pd_{0.45}Ni_{0.55}$. However, in

general, the transverse branches are not in good agreement with the experimental data as computed by using the TMMP. This discrepancy is due to the TMMP of Animalu which treats the pseudopotential in second-order perturbation theory and accounts for the two-body forces only while neglecting the contribution of the higher-order terms. So far, the phonon properties of $Pd_{0.45}Ni_{0.55}$ computed by two or three body interaction potentials have been presented. Hence, one of the aims of this study is to simulate Pd-Ni system by using many-body potentials and to see their effects on the lattice dynamical properties such as phonon dispersion curves and elastic constants.

The study of melting points, static structure, i.e., pair distribution function and static structure factor, and transport properties, such as diffusion and viscosity provides an understanding of behavior of liquid metals. Melting process of fcc transition metals has been investigated in several theoretical studies [11, 12, 13, 14, 15, 16]. Most of them are carried out by applying the embedded atom method (EAM) to metals. Foiles and Adams [11] determined the melting points (T_m) of Cu, Ag, Au, Ni, Pd and Pt from intersection of the solid and liquid free energies by using Monte-Carlo (MC) simulations. Melting points of Cu, Ag and Ni are consistent with experiments, but the model fails to describe T_m of the rest. The same method was applied to Al by performing molecular dynamics (MD) simulations by Mei and Davenport [12]. Their T_m result is below experimental value by about 130 K. MD simulations of Cu [13] and Ni [14] show that, using EAM, the system melts at 1370 K and 1705 K, respectively, compatible with

the experiments. Gomez *et al.* [15] studied the melting properties of nine fcc transition metals described by second-moment tight-binding method (SM-TBM) using a constant-pressure MC simulation. However, their results, except for Pb, do not agree with the experimental results. More recently, Cherne and Baskes [16] have calculated the melting temperature of Ni with two different EAM and four variations of the modified embedded atom model (MEAM) by using the moving interface method [17]. They found T_m below the experimental value for the EAM function, while above the experimental result, except one, for the MEAM functions. The melting temperatures of Pd-Ni alloys have not been computed up to now. The available experimental data for T_m of Pd-Ni alloys [18] present considerable challenge for a simulation work.

The transport properties (viscosity and diffusivity) are important for metallurgical processes as well as for understanding the dynamics of liquids. However, experimental data for the self-diffusivities of liquid metals are relatively scarce, mainly due to a lack of specific radio-isotopes. Experimental diffusion data are only available for about a dozen liquid metals [19]. Moreover there are variations between the experimental viscosity data [20]. The accurate measurement of these quantities is a difficult task due to difficult experimental conditions at high temperatures and pressures. In addition, available data are limited to a few specific temperatures. Moreover, little attention has been paid to temperature dependence of transport properties in theoretical studies. Hence, this study is also motivated by the fact that a comprehensive study of the temperature and

concentration dependence on the transport properties is required for Pd-Ni alloys.

When liquid metals are cooled down rapidly below their melting temperatures, they can be transformed into glasses. Amorphous metal glasses have been widely used because of their desirable properties, such as their extreme ductility and resistance to corrosion [21]. Knowledge of the microscopic processes of glass formation is essential for understanding and controlling materials properties.

Since the first amorphous metallic alloy was made by Duwez *et al.* [22], much research has been devoted to study the metallic glasses. Inoue reported three empirical rules for the achievement of high glass-forming ability in metallic glasses [23]. They served as a guiding principle for the selection of elements. It has been accepted that the mismatch in the atom size (significant difference in atomic size among the elements ratio above about 12 %) is one of the important factors in the glass forming process. Lu *et al.* [24] showed that the best glass forming alloys are those having eutectic composition or being very near to a eutectic composition. However, the issue of glass-forming ability of the metals is not yet fully understood. Therefore the understanding of their thermal, structural and dynamical properties is essential for the explanation of such a phenomenon. The metallic glass-forming alloys must be rapidly quenched with rates up to 10^{13} K/s^{-1}. However, the high cooling rate restricts the practical applications of the amorphousiation technique. Experiments have not allowed us to directly measure how an atom moves to a particular neighborhood in a glass. Therefore determination of the nature of glass formation by experiment is hardly possible.

Computer simulations provide an opportunity to understand the nature of the glass formation at an atomic level.

There are a large number of studies in MD simulation of glass transitions. The mismatch in atomic size is their common feature. Among these are studies on pure metals, such as Al [25, 26], Cu [26, 27], Au [28], Ni [28], and Rb [29], and binary metal-alloys including good glass formers like Ni-Al [30], Cu-Ag [31], and Au-Ni [32].

Pd-Ni metal alloy has a eutectic region around 45% of Pd. Pd and Ni have very different sizes, making them good candidates for forming a metal glass. Hence we are interested in the properties of metallic glass of $Pd_{0.45}Ni_{0.55}$.

It is necessary to implement the theoretical tools on the computer to meet our objectives. The most important problem in a computer simulation is to choose the interatomic potential model that provides an accurate description of atomic interactions. The local density plays a significant role in the interactions in metals and their alloys. Therefore, the model potential selected for transition metals should include many-body interactions as well as pairwise interactions. A wide range of models for atomic interactions have been developed. The first-principles molecular dynamics based on density functional theory introduced by Car and Parinello [33] is the most powerful method. This method studies one system in detail and supplies the most accurate information about the atomic interactions, but it needs considerable computer power and time to obtain the results. Computer limitations allow this method to simulate systems with only a

few hundred atoms. On the other hand, there are empirical and more practical approaches that can afford to investigate many systems and trends in physical properties. The empirical potentials provide a chance for studying systems with large number of atoms in a short time and with satisfactory accuracy. Some of these methods used in metallic systems are the effective-medium theory [34], the embedded-atom method [35] and the Finnis-Sinclair potential [36]. Recently, a many-body potential has been introduced by Sutton and Chen (SC) [37] within the context of the tight binding approach. This method describes the fcc metals well. Because of computational efficiency and fairly long-range properties, it has been used in many studies and successfully applied to a range of problems [38, 39, 40, 41, 42, 43, 44]. More recently, Çağın and co-workers have modified the Sutton-Chen (SC) type potential to include quantum corrections [45]. This potential has been applied to study various problems successfully ranging from alloys, glass formation, crystallization, clusters, nanowires, single crystal plasticity of pure metals, lattice dynamical and transport properties of fcc transition metals and their binary alloys [31, 46, 47, 48, 49, 50, 51, 52].

In this study, we have performed MD simulations using the SC potential and its new potential parameter set, quantum Sutton-Chen potential (Q-SC). This work investigates the solid, liquid, and solidification properties of Pd, Ni, and their binary alloys. The potential parameters for the binary alloys are obtained from some combination rules without any further fitting to alloy properties.

In solid phase, we are particularly interested in the concentration and temperature dependence of phonon dispersion relation and elastic constants to show the validity of potential energy function. The elastic constants are determined both from the long-wavelength limit of the phonon dispersion and from static deformation of unit cell by taking the second derivative of the total energy with respect to deformations. The enthalpy of mixing is also studied to investigate the nature of miscibility.

In liquid phase, the melting temperatures for Pd-Ni alloys are predicted by observing the discontinuity in the density and enthalpy, and the change in the pair distribution function and diffusion coefficients. Temperature and concentration dependence of the transport properties, such as the diffusion coefficient and viscosity are analyzed.

Empirical potentials are usually optimized to some experimental or first-principle results at solid phase. Whether the potential derived from elemental pure solid properties is able to describe the behavior of the liquid pure metals and especially binary alloys is not clear. Hence we are interested in testing the transferability of the potential from solid phase to liquid phase and from elemental case to metal alloys for Pd-Ni system. The results of the liquid and solid properties studied in this work are compared with the experimental data, where available, to measure the reliability and utility of the SC potential model.

For solidification process, the eutectic $Pd_{0.45}Ni_{0.55}$ concentration is quenched at different cooling rates to see whether the system goes into glass formation or

it crystallizes.

This thesis is arranged as follows: Chapter 2 consisting of three main sections offers some review to set up a background. MD method and SC potential model are summarized in Sections 2.1, and 2.2, respectively. The details of the computational procedure are given in Section 2.3. Chapter 3 contains our simulation results including solid and liquid properties, and solidification process, their subsequent analysis and discussion. Whenever possible, these results are compared with experimental values and other calculations. Finally, conclusion is presented in Chapter 4.

CHAPTER 2

METHOD

2.1 MOLECULAR DYNAMICS

Molecular Dynamics (MD) is a numerical simulation method calculating the time dependent behavior of the system. In this technique, the forces between atoms are calculated explicitly and the motion of an atom is computed using a suitable numerical integration method, essentially solving Newton's equation of motion. The algorithm consists of three essential parts; initialization, equilibrium, and production. Initialization requires specifying initial coordinates of the atoms and their velocities. A system of N particles is initially positioned within a cell of fixed volume, generally cubic in shape. A set of velocities are generated from random numbers, usually selected in such a way as to make the net momentum zero and its magnitude is scaled to the desired temperature. Following Newton's prescriptions, from the initial positions, velocities and forces, it is possible to calculate the positions and velocities of the atoms at small time interval Δt (a time step) later. The forces are re-calculated from these new positions and another step in time is made. The cycle has to be repeated many times in the course of a full simulation. System comes to equilibrium after a few thousands of the time steps, in which all memory of the initial configuration has been lost and settles

down to the desired equilibrium. Then a production period begins in which the trajectory of the atoms is stored for later analysis. Many thousands of time steps may be needed to produce a statistically accurate description of a phenomenon of interest. Hence, the thermodynamical properties can be calculated by averaging certain quantities over the equilibrium phase-space trajectory (ensemble average).

MD is a very powerful technique, but has some limitations. MD simulations are restricted by the speed and storage (memory) constraints of the available computers. Hence, simulations are usually performed on systems containing a few thousands of atoms, and for simulation times ranging from a few picoseconds to hundreds of the nanoseconds. Because of these size limitations, a cut-off is applied at a certain interatomic separation (R_c) and interactions between atoms separated by more than R_c are ignored in the calculation of the atomic forces. This results in enormous saving of computer resources. However, the imposition of the cut-off gives rise to a break in the continuity of the function at the cut-off distance R_c. This introduces the error in the numerical integration and energy conservation. The cure is to use the shifted potential energy U(r)=U(r)-U(R_c) to control the energy conservation [53]. A limited system size can also introduce surface effect problems. A solution to this problem is to use periodic boundary conditions (PBC) with minimum image convention [53, 54]. All the atoms are put inside a box called the unit cell. As an atom goes outside the cell boundary, its image is brought back in from the opposite side of the cell to replace it, and hence the total number of atoms is conserved. Infinite systems may be simulated

in this way. Because of the speed limitations, simulations are confined to the studies of the properties having short relaxation time. The relaxation time of the quantities we are interested in must be much smaller than the simulation time to get the physical properties accurately.

MD is constructed on classical approximation whose validity can be expressed by de Broglie thermal wavelength [55] defined as;

$$\lambda = \sqrt{\frac{2\pi\hbar}{Mk_BT}} \quad , \tag{2.1}$$

where M is the atomic mass and T is the temperature. The classical approximation is valid if $\lambda << a$, where a is the mean nearest neighbor distance. Hence MD simulations are poor for very light systems. Moreover, MD simulations are also unsuitable for low temperatures where quantum effects become important. The results should be interpreted with caution in these regions. The accuracy of the simulation results depends critically on a realistic choice of a potential energy function, which contains the physics of the model system.

There are several algorithms based on finite difference method [56] for performing the numerical integration of the equations of motion. This technique generates detailed phase space information such as atomic positions and velocities, at each time step, which is called the trajectory of the system. The Verlet algorithm is widely used because it requires a minimum amount of computer memory and CPU time. It uses the positions and accelerations of the atoms at the current time step and positions from the previous step to compute the positions for the next time step. The velocity Verlet algorithm uses positions,

velocities and accelerations at the current time step. This gives a more accurate integration than the Verlet algorithm. The Verlet and velocity Verlet algorithms often have a step in which the velocities are rescaled to correct for minor error in the integration. The predictor-corrector algorithm predicts the next set of positions and accelerations, then compares the accelerations to the predicted ones to compute a correction for the step. Each step can thus be refined iteratively. Predictor-corrector algorithms give an accurate integration but are seldom used due to their large computational needs.

The choice of a time step is also important. A time step that is too large causes atoms to move too far along a given trajectory, thus poor simulation of the motion. A time step that is too small makes it necessary to run more iterations, thus taking longer to run the simulation. Therefore, the time step should be one order of magnitude less than the time scale of the vibrational period or the time between collisions. This gives time step on the order of femtoseconds for simulating a liquid of rigid molecules and tenths of a femtosecond for simulating vibrating molecules [57] .

The computer program we have used in this study to perform MD simulation is introduced in the next section.

2.1.1 The Details of the Computer Program

The algorithm of our computer program is based on the extended Hamiltonian formalism arising from the works of Andersen [58], Parrinello-Rahman [59], Nosé [60], Hoover [61], and Ray and Rahman [62]. The details of the extended

Hamiltonian method are given in Section 2.1.2. Q-SC and SC potential parameters are used to define the interaction between atoms. We adopt the random binary fcc metal alloy method. The program initially requires the potential parameters, the number of atoms, density of the system, temperature, integration time step, Parrinello-Rahman piston mass and Nosé-Hoover thermostat mass parameters in the desired ensembles (HPN, TPN, EVN, and TVN). It selects a configuration randomly for the atomic positions arranged on a fcc lattice subject to periodic boundary conditions at the beginning of the simulation. The configuration chosen by the program may be unsuitable for the minimum energy configuration of the atoms, forming a drawback for the simulation. The initial velocities of the atoms are distributed randomly to obey the Maxwell-Boltzmann law. Fifth order Gear predictor-corrector algorithm, which is described in Section 2.1.3, is used to solve Newton's equation of motion with a time step Δt=0.002 ps. Parrinello-Rahman piston mass parameter W and Nosé-Hoover thermostat mass Q are chosen as 400 and 100, respectively [43, 44]. The cut-off distance for the interactions between the atoms is taken as two lattice parameters where the forces are negligibly small. An additional distance of half a lattice parameter is also added to this range to consider the temperature effect. Initially, the density of the alloy system is taken as a concentration average of the densities of elemental metals. The number of atoms N filling fcc lattice of cubic box is chosen, such that it satisfies $N = 4I^2$, where I is an integer. 864 and 1372 atoms

in the simulation box are preferred for efficiency and speed of our current computers which are Intel compatible Linux Workstation Pentium III and Pentium IV. The numerical procedures used by MD simulation program and the programs developed to analyze the trajectories of atoms are carried out in the FORTRAN language (FORTRAN 77+FORTRAN 90).

The trajectories are stored at a few time steps to compute some static and dynamical properties. MD also generates the averages, fluctuations and cross fluctuations of some thermodynamical properties, such as total energy (TE), potential energy (PE), kinetic energy (KE), pressure (P), virial, volume (V), etc. Other properties such as heat capacity c_p or c_v, isothermal compressibility β_T, and thermal expansion coefficient α_p can be evaluated by thermal fluctuations in different ensembles. For example, the constant-volume heat capacity is related to the total internal energy fluctuation, the constant-pressure heat capacity is related to enthalpy fluctuation, isothermal compressibility is connected with volume fluctuation, and thermal expansion is expressed in terms of the cross correlation of volume and enthalpy [54]. The MD computer program provides atomic information about the structure in terms of pair distribution function g(r), which are described in Section 2.3.3. The program also computes the elastic constants using statistical fluctuation formula given in Eq. 2.28.

2.1.2 Extended Hamiltonian Method

In a conventional MD simulation, the Newtonian equations of motion of a system with N particles in a fixed MD cell of volume V are integrated numerically. In

the absence of external perturbation, the total energy E and total linear momentum p are conserved, and thus the ensemble generated by the simulation is the microcanonical (EVN) ensemble. However, microcanonical ensembles are inappropriate for simulating certain systems which require constant pressure and/or temperature conditions. A constant temperature simulation may be required for determining how the behavior of the system changes with temperature, such as glass formation. Constant pressure simulation enables the behavior the system to be explored as a function of pressure, enabling one to study phase transitions. Many experimental measurements are made under conditions of constant temperature and pressure, so simulations in TPN ensemble are directly relevant to experimental data. Certain structural rearrangements are achieved more easily in an isobaric simulation than in a simulation at constant volume.

In certain applications, it is more convenient to perform simulations in other ensembles rather than EVN, such as isoenthalpic-isobaric (HPN), isothermal-isobaric (TPN), canonical (TVN), and grand canonical (μTV) ensembles, etc., where N, H, P, T, V, and μ denote, respectively, the number of particles, the enthalpy, the pressure, the temperature, the volume, and the chemical potential. In this study, the simulations are performed in the HPN, TPN, EVN, and TVN ensembles.

Several methods have been developed to perform dynamical simulations in different ensembles. One of them is the extended Hamiltonian method, which introduces additional degrees of freedom to represent the environment of the

macro-molecular system (e.g., pressure piston, thermostat etc.). The equations of motion for the extended system are expressed as augmented versions of the standard equations of motions to represent the evaluation of both the internal and external variables in the desired ensemble.

In this sense, most simulation methods originated from works of Andersen [58]. In the formulation of the constant pressure simulation method, an extra degree of freedom corresponding to the volume of the box V is added to the system. The kinetic energy and potential energy associated with this degree of freedom are

$$E_{kin} = \frac{1}{2} W \dot{V}^2 \tag{2.2}$$

and

$$E_{pot} = PV \quad , \tag{2.3}$$

respectively, where W is the mass of the piston, P is the desired pressure. The volume varies during the simulation with the average volume determined by the balance between the internal pressure of the system and the desired external pressure. Newton's equations are then solved for the extended system, i.e. the system of interest plus the piston, described by the fluctuating volume V and scaled coordinate $\vec{r}_i = V^{1/3}\vec{r}_i'$. The conserved quantity is no longer the sum of kinetic and potential energies of the particles, but, instead, the enthalpy of the system. Hence this method generates the constant enthalpy, constant pressure (HPN) ensemble.

Parrinello and Rahman [59] extended Andersen's constant pressure method to allow a change of size and shape of the simulation cell by introducing dynamical

variable matrix $\mathbf{h} = (\vec{h}_1, \vec{h}_2, \vec{h}_3)$, where $\vec{h}_1$, $\vec{h}_2$, and $\vec{h}_3$ are three vectors describing the size and changing shape of simulation cell. With the introduction of h matrix into the method, the studies of phase transition in crystalline solids and full description of the elastic properties of the system are easier to study. The scaled position vectors follows the equation;

$$\vec{r}_i = \mathbf{h}.\vec{r}_i' \quad . \tag{2.4}$$

The additional terms in the Hamiltonian are

$$E_{kin} = \frac{W}{2} \sum_i \sum_j Tr\tilde{\mathbf{h}}\mathbf{h} \tag{2.5}$$

and

$$E_{pot} = PV \quad , \tag{2.6}$$

where the cell volume is $V = |\mathbf{h}| = \vec{h}_1.\left[\vec{h}_2 \times \vec{h}_3\right]$. The equations of motion for the vector components are solved in exactly the same way as the equations for the positions, so that a new sample shape is generated at each time step.

Nosé [60] developed a dynamical method for controlling the temperature of the system by adding a heat bath with a degree of freedom denoted by s. The system is placed in a heat bath at temperature T. The system and the bath permit exchanging no particles but only energy. The system's temperature reaches to T when the equilibrium is attained. Since there is a thermal contact between the two, the total energy of the system fluctuates. The extended system is treated as an isolated system, i.e., its total energy is conserved. This forms a canonical ensemble (TVN). The kinetic and potential energies of the heat bath are defined

as;

$$E_{kin} = \frac{1}{2} Q \left(\frac{ds}{dt} \right)^2 = \frac{p_s^2}{2Q} \tag{2.7}$$

and

$$E_{pot} = g k_B T \ln(s) \quad , \tag{2.8}$$

respectively, where p_s is the conjugate momentum of s. Q is a parameter of dimension energy$\times$(time)^2 and behaves as a mass for the motion of s, k_B is Boltzmann's constant, T is the externally set temperature, and the parameter g is essentially equal to the number of degrees of freedom of the physical system. The extended system produces the following scaled coordinates;

$$\begin{aligned} \vec{r_i} &= \vec{r_i'} \quad , \\ \vec{p_i} &= \frac{1}{s} \vec{p_i'} \quad , \\ dt &= \frac{1}{s} dt' \quad , \end{aligned} \tag{2.9}$$

where $'$ denotes the coordinates of virtual extended system.

Hoover [61] has shown that the equations derived by Nosé can be further simplified by introducing the thermodynamic friction coefficient of the bath $\eta = sp_s/Q$. The equations of motion then become as;

$$\begin{aligned} \dot{\mathbf{r}}_i &= \mathbf{p}_i / m_i \quad , \\ \dot{\mathbf{p}}_\mathbf{i} &= \mathbf{F_i} - \eta \mathbf{p_i} \quad , \\ \dot{\eta} &= \frac{\sum_i p_i^2/m_i - g k_B T}{Q} \quad . \end{aligned} \tag{2.10}$$

The friction coefficient is not a constant and can take on both positive and negative values, leading to a negative feedback mechanism. The last term in Eq. 2.10

controls the functioning of the heat bath. From this equation we observe that if the total kinetic energy is greater than gk_BT, then $\dot{\eta}$ is positive. This creates a friction inside the bath and hence the motion of the atoms are decelerated to lower their kinetic energy to that of the heat bath. On the other hand, if the kinetic energy is lower than gk_BT then $\dot{\eta}$ is negative, and correspondingly the bath is heated up and accelerate the atoms. Eqs. 2.10 are collectively referred to as the Nosé-Hoover thermostat [63].

We have used the method developed by Ray and Rahman [62] for TPN dynamics, which combines Nosé constant-temperature theory with Parrinello-Rahman variable shape-size form of MD. The Hamiltonian for the TPN dynamics of MD has the form;

$$\begin{aligned} H(r^{'}, p^{'}, h, \Pi, s, p_s) &= \sum_i \frac{\tilde{p_i}^{'} G^{-1} \tilde{p_i}^{'}}{2m_i s^2} + U + \frac{Tr(\tilde{\Pi}\Pi)}{2W} + V_0 P \\ &+ \frac{p_s^2}{2Q} + (3N+1)k_B T_0 \ln(s) \quad , \end{aligned} \tag{2.11}$$

where $(r_i^{'}, p_i^{'})$ are the scaled coordinate and its conjugate momentum. They are related to physical particle position and momentum (r_i, p_i) by $r_i = hr_i^{'}$ and $p_i = \tilde{h}^{-1} p_i^{'}/s$, respectively. (h, Π) are the coordinate and momentum of the molecular dynamics cell arising from Parinello and Rahman expression and (s, p_s) are the Nosé mass scaling variable and its conjugate momentum. The masses W and Q are the parameters to obtain dynamical equations for the variables h and s. The tilde indicates matrix transpose. U is the potential energy of the atoms. T_0 is the thermal reservoir temperature. P is the desired pressure related by strain matrix

$$\varepsilon = (\tilde{h_0}^{-1} G \tilde{h_0}^{-1} - 1)/2 \quad , \tag{2.12}$$

where G is the metric tensor, $G = \tilde{h}h$ and h_0 is the reference state of the cell matrix h at zero pressure. V_0 is the reference volume calculated from $V_0 = det(h_0)$. The first two terms in Eq. 2.11 is the Hamiltonian for N particles in the simulation system, the second two terms refers to molecular dynamics cell and the last two terms represents the contribution originated from Nosé constant temperature theory.

There are 3N+9+1 equations of motion to be solved for TPN dynamics (N is the number of particles with 3 degrees of freedom, h matrix has 9 independent components, and one more degree of freedom of s). The equations of motion of the other three dynamics can be evaluated from TPN dynamics by applying some constraints. If the Nosé variable s satisfies $\dot{s} = 0$, $s = 1$, TPN dynamics is reduced to HPN dynamics. Similarly, constraint on $\dot{h} = 0$, h =constant give rise to TVN dynamics. If s and h satisfy $\dot{s} = 0$, $s = 1$ and $\dot{h} = 0$, h =constant, EVN dynamics is obtained.

2.1.3 Gear Predictor-Corrector Algorithm

Predictor-Corrector algorithm is composed of three steps; prediction, evaluation and correction. Since the trajectory of the atomic motions is a continuous function of time, position and its derivatives at time $t + \Delta t$ can be expanded as Taylor series up to fifth order and predicted as follows;

$$\begin{aligned} r_i^P(t+\Delta t) &= r_i(t) + \dot{r}_i(t)\Delta t + \frac{\ddot{r}_i(t)}{2!}(\Delta t)^2 + \frac{r_i^{(iii)}(t)}{3!}(\Delta t)^3 \\ &+ \frac{r_i^{(iv)}(t)}{4!}(\Delta t)^4 + \frac{r_i^{(v)}(t)}{5!}(\Delta t)^5 \quad , \end{aligned}$$

$$
\begin{aligned}
\dot{r}_i^P(t+\Delta t) &= \dot{r}_i(t) + \ddot{r}_i(t)\Delta t + \frac{r_i^{(iii)}(t)}{2!}(\Delta t)^2 + \frac{r_i^{(iv)}(t)}{3!}(\Delta t)^3 \\
&+ \frac{r_i^{(v)}(t)}{4!}(\Delta t)^4 \quad , \\
\ddot{r}_i^P(t+\Delta t) &= \ddot{r}_i(t) + r_i^{(iii)}(t)\Delta t + \frac{r_i^{(iv)}(t)}{2!}(\Delta t)^2 + \frac{r_i^{(v)}(t)}{3!}(\Delta t)^3 \quad , \qquad (2.13) \\
r_i^{(iii)P}(t+\Delta t) &= r_i^{(iii)}(t) + r_i^{(iv)}(t)\Delta t + \frac{r_i^{(v)}(t)}{2!}(\Delta t)^2 \quad , \\
r_i^{(iv)P}(t+\Delta t) &= r_i^{(iv)}(t) + r_i^{(v)}(t)\Delta t \quad , \\
r_i^{(v)P}(t+\Delta t) &= r_i^{(v)}(t) \quad .
\end{aligned}
$$

The forces at time $t+\Delta t$ are evaluated by taking the gradient of the potential at the new predicted position $r_i^P(t+\Delta t)$ and in turn the acceleration $\ddot{r}_i^C(t+\Delta t)$, which can be used as a corrector. By means of this corrector, it is possible to estimate the error in the predicted acceleration $\ddot{r}_i^P(t+\Delta t)$ as follows;

$$
\Delta\ddot{r}_i(t+\Delta t) = \Delta\ddot{r}_i^C(t+\Delta t) - \Delta\ddot{r}_i^P(t+\Delta t) \quad . \qquad (2.14)
$$

The corrected equations are obtained by adding this difference term to the predicted values,

$$
\begin{aligned}
r_i^C(t+\Delta t) &= r_i^P(t+\Delta t) + c_0\Delta\ddot{r}_i(t+\Delta t) \quad , \\
\dot{r}_i^C(t+\Delta t) &= \dot{r}_i^P(t+\Delta t) + c_1\Delta\ddot{r}_i(t+\Delta t) \quad , \\
\ddot{r}_i^C(t+\Delta t) &= \ddot{r}_i^P(t+\Delta t) + c_2\Delta\ddot{r}_i(t+\Delta t) \quad , \qquad (2.15) \\
r_i^{(iii)C}(t+\Delta t) &= r_i^{(iii)P}(t+\Delta t) + c_3\Delta\ddot{r}_i(t+\Delta t) \quad , \\
r_i^{(iv)C}(t+\Delta t) &= r_i^{(iv)P}(t+\Delta t) + c_4\Delta\ddot{r}_i(t+\Delta t) \quad , \\
r_i^{(v)C}(t+\Delta t) &= r_i^{(v)P}(t+\Delta t) + c_5\Delta\ddot{r}_i(t+\Delta t) \quad ,
\end{aligned}
$$

where c_α are the coefficients determined by Gear [64] so as to achieve the best

accuracy and stability.

2.2 EMPIRICAL POTENTIALS

2.2.1 Introduction

The description of atomic interactions, the so-called interatomic potential, can be modeled by several methods, ranging from first-principle to empirical potentials. The success of any atomistic simulations depends on choosing an accurate and transferable model for the interatomic potential. The most computationally efficient method for large systems is the use of the empirical interatomic potentials. These potentials are obtained by fitting the potential parameters to some experimental properties of the material.

Pair potentials are usually used to simulate metallic systems. These simple potentials alone are very successful but insufficient to describe metallic bonding which is due to the sharing of the electrons in the system and neglects the physics of metallic bonding. For example, pair potentials gives the Cauchy relation of the elastic constants, $C_{12} = C_{44}$, which does not hold for metals. Volume dependent cohesive energy term [65] is added to the pair potential energy to improve the description of elastic properties of the solids, but this results in a trouble that the bulk modulus calculated by the method of long waves differs from its value calculated by homogeneous deformations. Another drawback of the use of pair potentials is to overestimate the vacancy formation energies, whose values come out to be nearly equal to the cohesive energies. However, the experimental data

suggest that the vacancy formation energy for metals is about one third of the cohesive energy. Moreover, pair potential models fail to predict the melting point which differ by more than 20 % of the experimental value. The surface structure and relaxation properties also can not be properly described by means of pair potentials.

Some empirical potentials have been proposed to overcome these problems faced by pair potentials by introducing a new term based on the concept of local density accounting for the many-body effects. The embedded atom model (EAM) [35] and the Finnis-Sinclair (FS) model [36] are the ones used widely for transition metals. Both of these potentials are based on similar expressions for the total energy of the system of N atoms;

$$U = \frac{1}{2}\sum_{i}\sum_{j\neq i}^{N} V(r_{ij}) + \sum_{i}^{N} f(\rho_i) \quad , \tag{2.16}$$

where $V(r)$ is a two-body part describing electrostatic contribution and $f(\rho)$ is a function giving the energy of an atom as a function of a generalized coordination ρ. ρ is constructed as a superposition of contributions from neighbor atoms;

$$\rho_i = \sum_{i}^{N} \phi_i(r_{ij}) \quad , \tag{2.17}$$

where $\phi_i(r_{ij})$ is a short-ranged function of distance.

Even if these two potentials share the same analytical form, their physical interpretation are different, resulting in different functions for $V(r)$, $\phi(r)$, and $\rho(r)$. From the point of view of EAM, the energy of the system is determined by the use of density functional theory [67, 68]. The cohesive energy of a metallic

system is expressed in terms of embedding energies $f(\rho)$ obtained by empirical fitting. That is, each atom in the metal is embedded into the electron gas created by the other atoms. The EAM has been applied to a wide-range of physical problems successfully, but it has very complicated form and sometimes a simple analytical form is not even available. On the other hand, FS potential is based on the analogy [69] with the second moment approximation to the tight binding model. The cohesive energy of a solid is proportional to the square root of its atomic coordination number and $\phi(r)$ can be interpreted as a sum of squares of hopping (overlap) integrals [70]. The empirical FS potential has simple form and works well for transition metals, but its interaction range is very short, such that it does not describe the surface properties adequately.

In this work, the Sutton-Chen (SC) potentials developed for long range force field of fcc metals are used as an interatomic potential to define interactions between the atoms. The details of the potential are given in the following section.

2.2.2 Sutton-Chen Many-Body Potential

The SC potential [37], long range FS potential for elemental transition metals in comparison to EAM potentials, consists of a pairwise repulsive part and many-body attractive part. The long range nature of the potential is due to using simple inverse power forms for the functions $V(r)$ and $\phi(r)$ given by Eqs. 2.16 and 2.17, respectively. The total potential energy of the metals and their binary alloys has

the following form;

$$U = \sum_i U_i = \sum_i \left[\sum_{j \neq i} \frac{1}{2} \epsilon_{ij} V(r_{ij}) - c_i \epsilon_{ii} \left(\rho_i\right)^{\frac{1}{2}} \right] \quad , \tag{2.18}$$

where $V(r_{ij})$ is a repulsive pairwise potential describing long range interaction with a van der Walls tail between the i th and j th atomic cores;

$$V(r_{ij}) = \left(\frac{a}{r_{ij}} \right)^n \quad , \tag{2.19}$$

and ρ_i is a local energy density responsible for cohesive many-body interaction at short range associated with atom i, and it is given as;

$$\rho_i = \sum_{j \neq i} \phi(r_{ij}) = \sum_{j \neq i} \left(\frac{a}{r_{ij}} \right)^m \quad . \tag{2.20}$$

In the Eqs. 2.18- 2.20, r_{ij} is the distance between atoms i and j, a is a parameter with the dimension of length and is generally taken to be the equilibrium lattice constant, c is the positive dimensionless parameter scaling the cohesive term relative to repulsive term, ϵ sets the overall energy scale and n, m are positive integers with $n > m$. The SC parameters are obtained by fitting to some solid state properties based on the experimental lattice parameter, cohesive energy, and bulk modulus. The indices m and n are restricted to integer values, such that the product mn is the nearest integer to $18\Omega^f B^f / E^f$ as given in Ref. [37], where Ω^f is the fcc atomic volume, B^f is the bulk modulus, and E^f is the cohesive energy.

The SC potentials have been generalized for random binary fcc metal alloys by Rafii-Tabar and Sutton [71]; two types of atoms occupies the sites completely randomly. A mixing rule which reflects different averaging procedures, such as

the arithmetic or the geometric averaging is proposed to describe the energy of the binary $i-j$ alloys, where i and j are elemental metals;

$$V(r_{ij}) = \sqrt{V(r_{ii})V(r_{jj})} \tag{2.21}$$

and

$$\phi(r_{ij}) = \sqrt{\phi(r_{ii})\phi(r_{jj})} \quad , \tag{2.22}$$

leading to the alloy parameters as;

$$\epsilon_{ij} = \sqrt{\epsilon_i \epsilon_j} \quad , \tag{2.23}$$

$$m_{ij} = \frac{m_i + m_j}{2} \quad , \tag{2.24}$$

$$n_{ij} = \frac{n_i + n_j}{2} \quad , \tag{2.25}$$

$$a_{ij} = \frac{a_i + a_j}{2} \quad . \tag{2.26}$$

The criterion for selecting the mixing rule is the consistency of the results obtained with the corresponding experimental values. SC potentials have the advantage that all the parameters for the alloys are obtained from those for the elemental metals without the introduction of any new parameters.

Rafii-Tabar and Sutton calculated the elastic constants and the enthalpy of mixing ΔH by lattice summation method after choosing the equilibrium lattice parameter a at 0 K of the random alloy as universal scale and expressing cohesive energy of random alloy in terms of a. The enthalpy of mixing ΔH per atom at 0 K can be obtained from

$$\Delta H = E_{A_{1-x}B_x} - (1-x)E_A - xE_B \quad , \tag{2.27}$$

Table 2.1: Quantum Sutton-Chen (Q-SC) [45] and Sutton-Chen (SC) [71] potential parameters.

metal	model	n	m	ϵ (eV)	c	a (A^o)
Pd	Q-SC	12	6	3.2864×10^{-3}	148.205	3.8813
	SC	12	7	4.1260×10^{-3}	108.526	3.8900
Ni	Q-SC	10	5	7.3767×10^{-3}	84.745	3.5157
	SC	9	6	1.5714×10^{-3}	39.756	3.5200

where E is the cohesive energy per atom and x is the concentration of B in A.

Recently, Çağın and co-workers [45] have reparametrized the SC potential by including quantum corrections accounting for zero-point energy to improve the results of the potential for elevated temperatures. Hence this modified set of SC potential is referred as quantum Sutton-Chen (Q-SC) potential. The Q-SC potential parameters are optimized to fit to some experimental properties in addition to the original SC parameters, such as phonon frequencies at the X point (at room temperature), vacancy formation energy and surface energies. The parameters used in this simulation are listed in Table 2.1.

2.3 COMPUTATIONAL PROCEDURE

Our simulations are composed of two main parts: heating and cooling processes. Three successive simulations are performed for heating processes of Pd-Ni alloys (Pd_xNi_{1-x}, where x=0, 0.1, 0.2, ..., 1 and x=0.45). First, HPN MD simulation is carried out to heat the system from 0.1 K to 3000 K with increments of 200 K for solid phase, 100 K for liquid phase. This increment is reduced to 10 K near the melting temperature to get more accurate values of the melting

temperature. The heating procedure is carried out by scaling velocities with the ratio of the increment temperature to the specific number of steps depending on target temperature, (1 K/step). At each temperature, 2000 time steps are carried out for equilibrium. Then 20000 additional steps in TPN dynamics are taken to obtain some statistical properties, such as volume, density and energy of the system. Finally, 50000 steps of EVN dynamics follows by using the resulting zero strain average matrix $< h_0 >$ to obtain pressure dependent properties of the system, such as elastic constant, phonon dispersion relation, diffusivity and viscosity.

The cooling process are carried out by using TPN and TVN MD dynamics. First, the $Pd_{0.45}Ni_{0.55}$ alloy (eutectic composition expected to be glass forming) is equilibrated at the temperature of 3000 K, where the liquid forgets its initial configuration. After that 50000 time steps of TPN dynamics is carried out. Then the system is cooled from 3000 K to 100 K with decrement of 100 K. We quench the system with the TPN ensemble for MD steps of 10000, 50000, 100000 and 1000000 at the same temperature, corresponding to cooling rates of 5×10^{12}, 1×10^{11}, 5×10^{11}, and 5×10^{10} K/s, respectively. Some macroscopic description of the system, such as volume, energy and structure are obtained from the TPN MD cooling runs. The TVN simulations depend on the TPN simulation results. The densities obtained from TPN cooling runs for each cooling rate are utilized as input parameters to perform TVN simulations. 5000 time steps are carried out for equilibrium of the system for each cooling rate to consider the effects of

the sudden volume changes. Finally, production runs are performed to obtain pressure dependent properties, such as shear viscosity.

In the following sections, some useful formulae used in our computations are given.

2.3.1 Elastic Constants

The zero strain state, h_0, of the system is determined to obtain the reference size and shape of the unit cell by performing TPN simulation with the stress equal to zero in our simulations. This reference state is used in EVN dynamics simulations to compute elastic constants, evaluated by using the following formula [72];

$$\begin{aligned} C_{ijkl} &= \frac{V_0}{k_B T}\left(< P_{ij}P_{kl} > - < P_{ij} >< P_{kl} >\right) \\ &+ \frac{2Nk_BT}{V_0}\left(\delta_{ik}\delta_{jl} + \delta_{il}\delta_{jk}\right) + < \chi_{ijkl} > \quad , \end{aligned} \tag{2.28}$$

where $V_0 = deth_0$ is the reference volume for the system. The first term represents the contribution from the fluctuation of the microscopic stress tensor, P_{ij}, the second term refers to kinetic energy contribution and the third term is the Born term related to hypervirial tensor, χ_{ijkl}. The expressions for tensors P_{ij} and χ_{ijkl} including the contribution from SC many-body potential have been described elsewhere [43, 44].

2.3.2 Phonon Dispersion Relation

The total potential energy U_{tot} can be expanded in terms of atomic displacements when we consider small vibrations of the atoms about their equilibrium position. In the harmonic approximation, the total potential energy of a crystal can be written as [73, 74];

$$U = \frac{1}{2} \sum_{\lambda l} \sum_{\nu l'} \frac{\partial^2 U}{\partial u_{\alpha,\lambda l} \partial u_{\beta,\nu l'}} u_{\alpha,\lambda l} u_{\beta,\nu l'} \quad , \tag{2.29}$$

where $u_{\alpha,\lambda l}$ is the displacement of the λ th atom in the l th unit cell in the direction α from its equilibrium position. Then the force constants

$$\Phi_{\alpha\beta} \begin{pmatrix} l & l' \\ \lambda & \nu \end{pmatrix} = - \left[\frac{\partial^2 U}{\partial u_{\alpha,\lambda l} \partial u_{\beta,\nu l'}} \right]_0 \quad , \tag{2.30}$$

can be calculated directly in terms of the calculated total energy U. It simply means the force exerted on the λ th atom in the l th unit cell in the α direction when the ν th atom in the l' th unit cell is displaced a unit distance in the β direction. In Eq. 2.30 the subscript 0 denotes that the derivatives are evaluated at the equilibrium positions.

The vibration frequencies of phonon can be obtained by solving the secular equation;

$$det \left| D_{\alpha\beta,\lambda\nu}(q) - w^2 \delta_{\alpha\beta} \delta_{\lambda\nu} \right| = 0 \quad , \tag{2.31}$$

where w is the angular frequency of the vibration, $\delta_{\alpha\beta}$ is the Kronecker symbol and $D_{\alpha\beta,\lambda\nu}$ is an element of the so-called dynamical matrix [75];

$$D_{\alpha\beta,\lambda\nu}(q) = \frac{1}{(m_\lambda m_\nu)^{\frac{1}{2}}} \sum_{l'} \Phi_{\alpha\beta} \begin{pmatrix} l & l' \\ \lambda & \nu \end{pmatrix} exp\left(i\vec{q}.\left[\vec{r}(\nu,l') - \vec{r}(\lambda,l)\right]\right) \quad , (2.32)$$

where m_λ is the mass of the λ th atom and $\vec{q}$ is the wave vector of the crystal vibration, l refers to the reference unit cell, l' denotes the neighbor unit cell.

The many body force on atom i along direction α $(= x, y, z)$ can be calculated as the gradient of the potential given in Eq. 2.18 [43, 44];

$$F_{i\alpha} = -\epsilon \left[\sum_{i \neq j} V'(r_{ij}) \frac{r_{ij\alpha}}{r_{ij}} - \frac{c}{2} \frac{\sum_{i \neq j} \phi'(r_{ij}) \frac{r_{ij\alpha}}{r_{ij}}}{\rho_i} + \sum_{i \neq j} \frac{c}{2\rho_j} \phi'(r_{ij}) \frac{r_{ij\alpha}}{r_{ij}} \right] \quad , (2.33)$$

where $'$ denotes $\frac{\partial}{\partial r_{ij}}$. Hence the force constant can be computed by taking first derivative of the many body force;

$$\begin{aligned}
\Phi_{\alpha\beta}(i,j) = & - \epsilon \left[\left(V''_{ij} - V'_{ij} \right) \Delta r_{ij\alpha} \Delta r_{ij\beta} + V'_{ij} \frac{\delta_{\alpha\beta}}{r_{ij}^2} \right] \\
& - \frac{\epsilon c}{4\rho_i^{3/2}} \left(\sum_{k \neq i} \phi'_{ik} \Delta r_{ik\alpha} \right) \phi'_{ij} \Delta r_{ij\beta} \\
& + \frac{\epsilon c}{2\rho_i^{1/2}} \left[\left(\phi''_{ij} - \phi'_{ij} \right) \Delta r_{ij\alpha} \Delta r_{ij\beta} + \phi'_{ij} \frac{\delta_{\alpha\beta}}{r_{ij}^2} \right] \\
& + \frac{\epsilon c}{4\rho_j^{3/2}} \phi'_{ij} \Delta r_{ij\alpha} \left(\sum_{k \neq j} \phi'_{jk} \Delta r_{jk\beta} \right) \\
& + \frac{\epsilon c}{2\rho_j^{1/2}} \left[\left(\phi''_{ij} - \phi'_{ij} \right) \Delta r_{ij\alpha} \Delta r_{ij\beta} + \phi'_{ij} \frac{\delta_{\alpha\beta}}{r_{ij}^2} \right] \\
& + \frac{1}{4} \sum_{k \neq i,j} \left[\frac{\epsilon c}{\rho_k^{3/2}} \left(\phi'_{ik} \Delta r_{ik\alpha} \phi'_{jk} \Delta r_{jk\beta} \right) \right] \quad .
\end{aligned} \quad (2.34)$$

Here $'$ is $r_{ij}\frac{\partial}{\partial r_{ij}}$, $''$ refers to $r_{ij}^2 \frac{\partial^2}{\partial r_{ij}^2}$. i is the index for the λ *th* atom of the l *th*

lattice cell (λ, l) and j is the index for the ν th atom of $l^{'}th$ lattice cell $(\nu, l^{'})$. Δr_{ij} is written as;

$$\Delta r_{ij\alpha} = \frac{r_{\alpha i} - r_{\alpha j}}{r_{ij}^2} \quad , \tag{2.35}$$

where $r_{\alpha i}$ is the α component of the position of the atom i.

The force constants should satisfy the following symmetry conditions arising from commutative of the partial differentiation and from Newton's third law;

$$\phi_{\alpha\beta}(i,j) = \phi_{\beta\alpha}(j,i) \tag{2.36}$$

and

$$\phi_{\alpha\beta}(i,i) = -\sum_{j \neq i} \phi_{\alpha\beta(i,j)} \quad . \tag{2.37}$$

It follows from these two rules that;

$$\sum_{j \neq i} \phi_{\alpha\beta}(i,j) = \sum_{j \neq i} \phi_{\beta\alpha}(i,j) \quad . \tag{2.38}$$

We have computed the interatomic force constants to obtain the phonon dispersion curves using the trajectories of the EVN dynamics. The symmetry conditions for the force constants have been checked to verify the force constant values. The system size for the alloy, 864 atoms, is insufficient for obeying the symmetry rules for the force constants. Therefore we construct the dynamical matrix composed of 12×12 elements by using 1372 atoms (7×7×7 cubic system) for the alloy system for the high symmetry directions in the first Brillouin zone. The LAPACK subprogram is used to diagonalize the dynamical matrix to obtain the eigenvalues giving the square of the angular velocity.

2.3.3 Pair Distribution Function

Pair distribution function $g(r)$ characterizes the static description of structural and thermodynamical properties. It can be defined as the probability of finding an atom at a distance from the atom at the origin. The area under the first peak of $g(r)$ can be described as the number of nearest-neighbor atoms. It is an important parameter for liquids, because their properties can be described in terms of the first coordination number. In MD simulations, it can be expressed as [54];

$$g(r) = \frac{V}{N^2} \left\langle \sum_i \sum_{i \neq j} \delta(r - r_{ij}) \right\rangle \quad . \tag{2.39}$$

Fourier transform of $g(r)$ provides us with the static structure factor S(q);

$$S(q) = \frac{1}{N} \left\langle \sum_{i=1} \sum_{j=1} exp[-i\vec{q}.(\vec{r}_i - \vec{r}_j)] \right\rangle \quad , \tag{2.40}$$

where $\vec{q}$ is a wave vector compatible with the periodic boundary conditions i.e., $\vec{q} = \left(\frac{2\pi}{L}\right)(n_x, n_y, n_z)$, where L is the length of the simulation box and n_α are integers.

2.3.4 Diffusion and Viscosity

Mass transport on an atomic scale, *i.e.*, atomic self diffusion, is one of the most characteristic properties of a liquid and plays a significant role in some processes such as corrosion, phase separation, crystal growth, and heterogeneous reactions, *etc.* In the MD simulations, the self-diffusion coefficients D can be determined either from an integral over the velocity auto-correlation function $C_v(t)$ using

Green-Kubo relation (GK) [54];

$$D = \frac{1}{3}\int_0^\infty C_v(t)dt \quad , \tag{2.41}$$

where

$$C_v(t) = \frac{1}{N}\left\langle \sum_{i=1}^{N} \vec{v}_i(t).\vec{v}_i(0) \right\rangle \quad , \tag{2.42}$$

or from the long time behavior of mean square displacement $r^2(t)$ by means of the Einstein relation (E);

$$D = \lim_{t\to\infty} \frac{r^2(t)}{6t} \quad , \tag{2.43}$$

where

$$r^2(t) = \frac{1}{N}\left\langle \sum_{i=1}^{N} [\vec{r}_i(t) - \vec{r}_i(0)]^2 \right\rangle \quad . \tag{2.44}$$

In the Eqs. 2.42 and 2.44, $v_i(t)$ is the velocity and $r_i(t)$ is the position of the $i\ th$ particle at time t.

The viscosity of the liquid metals is of great importance in metallurgical processes, such as refining, welting, casting, and solidification, as well as in the study for dynamics of atoms in the liquid metals. Shear viscosity is due to the velocity gradient which exists between parallel flux within a system. That is, it can be defined as the resistance of the liquid to flow. The evaluation of the shear viscosity is based on the determination of the microscopic stress tensor whose elements are given by [54];

$$P_{\alpha\beta} = m\sum_{i=1}^{N} v_{i\alpha}v_{i\beta} + \frac{1}{2}\sum_{i\neq j}^{N} r_{ij\beta}F_{ij\alpha} \quad , \tag{2.45}$$

where α, β are the Cartesian components (x, y, z), $v_{i\alpha}$ is the α component of the velocity of atom i, $r_{ij\beta}$ is the β component of the interatomic distance r_{ij}, and

$F_{ij\alpha}$ is the α component of the force exerted on atom j by the atom i. Shear viscosity η is determined from the stress auto-correlation function formed from the off-diagonal elements of the stress tensor by using Green-Kubo relation;

$$\eta = \frac{V}{k_B T} \int_0^\infty dt \sum_{\alpha\beta} \langle P_{\alpha\beta}(t) P_{\alpha\beta}(0) \rangle \quad , \tag{2.46}$$

where V is the total volume of the system. The summation is over the cyclic indicess $\alpha\beta = xy, yz,$ and zx. $<>$ in the correlation functions given by Eqs. 2.42, 2.44, and 2.46 denotes the average over 50 time origins along a trajectory. The simulation of self-diffusion coefficient and shear viscosity are performed by using EVN ensemble. The results are obtained by using an average of 2000 individual correlation functions spaced 0.002 ps.

2.3.5 Neighbor List Correlation Function

An atom's immediate surrounding are described as the nearest neighbors making a contribution to the first peak in the pair correlation function, $g(r)$. The event that the atoms in a system most likely leave their immediate surrounding and have a slightly different group of atoms surrounding them indicates that the diffusion process takes place [76].

The track of each atom's neighbors obtained from the trajectories of the atoms can be kept by neighbor list correlation function, $C_\ell(t)$, defined as;

$$C_\ell(t) = \frac{< \ell_i(0).\ell_i(t) >}{< \ell_i(0)^2 >} \quad , \tag{2.47}$$

where $\ell_i(0)$ is the neighbor list at time zero calculated up to distance r_{cut}, the location of the first minimum in the pair correlation function, for the atom i

centered at the origin, and $\ell_i(t)$ refers the new neighbor list at time t calculated up to the distance $r_{cut}+r_\ell$, where r_ℓ is added to r_{cut} to consider the vibrational effects if the neighbor list of an atom at time t is identical to the neighbor list at time zero, the correlation function has a value of 1 for that atom. If any of the original neighbors are missing at time t, it is assumed that the atom participate in diffusion event and the correlation function is 0.

CHAPTER 3

RESULTS AND DISCUSSION

3.1 SOLID PROPERTIES

3.1.1 Enthalpy of Mixing

The study of enthalpy of mixing is of great importance in the investigation of alloy miscibility. Enthalpy of mixing ΔH is calculated at 1300 K in solid phase and at 1900 K in liquid phase by using Q-SC potential, and the results are shown in Fig. 3.1. Experimentally, ΔH at solid phase is positive from pure Ni to the $Pd_{0.6}Ni_{0.4}$ concentration. The Pd-Ni alloy is a miscible system (negative enthalpy of mixing) after this concentration [18]. However, our result of solid phase is in the positive region. The fluctuation shown in the graph is due to considering only one configuration of the atoms. Moreover, in the liquid phase, the sign of the simulated ΔH is negative at all concentrations of the alloy system becoming energetically favorable, which is contrary to the experiment. The enthalpy of mixing is sensitive to permission of local relaxations, as has been pointed out in the study of Ackland and Vitek [77]. The system is allowed to be relaxed in this study. One of the reasons for the differences between the simulation and the experiment is the potential parameters fitted to pure metal properties, not to alloy properties. Also, the potential parameters are optimized to only 0 K

physical properties. Another reason for the disagreement with the experiment may be the usage of random fcc-alloy model.

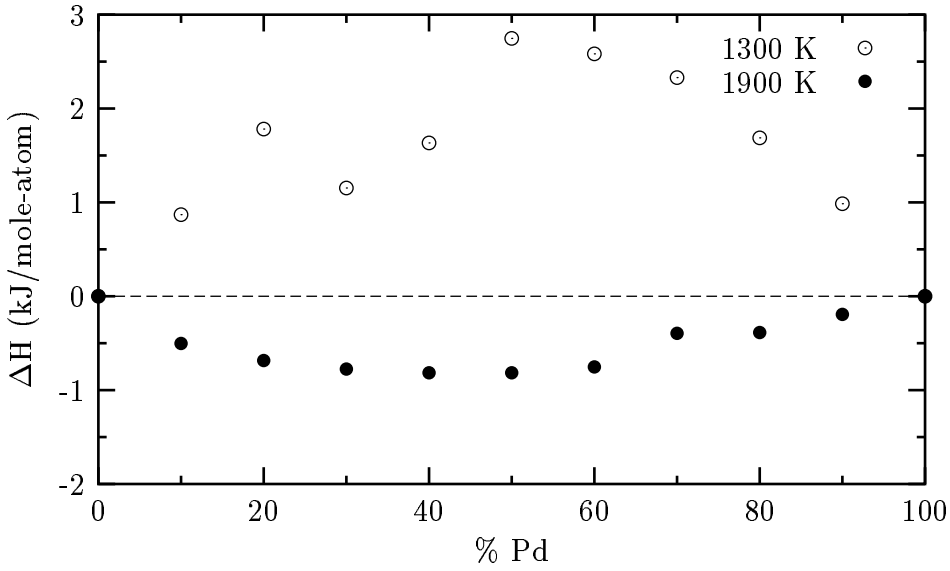

Figure 3.1: Enthalpy of mixing of Pd-Ni system at two different temperatures.

3.1.2 Thermodynamical Properties

Table 3.1 shows some thermodynamical properties, namely density (ρ), lattice constant (a_0), cohesive energy (E_c) and compressibility (κ) of Pd and Ni metals calculated by using SC and Q-SC potentials parameters at 300 K, together with a comparison with experimental data [78]. Q-SC description leads to improvement over the results obtained from SC potentials, except for the compressibility, as seen in Table 3.1. The discrepancy between Q-SC and experimental values for the first three properties is less than 1 %, for compressibility of Pd 12.5 % and for

Table 3.1: Density (ρ), lattice constant (a_0), cohesive energy (E_c), and compressibility (κ) of Pd and Ni metals calculated from Q-SC and SC potential parameters at 300 K, along with the available experimental data [78].

	Pd			Ni		
	Exp.	Q-SC	SC	Exp.	Q-SC	SC
ρ (g/cm^3)	12.038	11.955	11.813	8.907	8.886	8.745
a_0(A^0)	3.89	3.90	3.91	3.52	3.53	3.55
-E_c (kJ/mole)	376.0	370.2	372.5	428.0	424.0	420.6
κ (10^{-11}m^2/N)	0.553	0.622	0.537	0.538	0.576	0.550

that of Ni 7 %. We expect that the results of compressibility will be improved at high temperatures because Q-SC potential describes well temperature dependent properties. It is worth noting that although a_0 is set to be the experimental lattice parameter at room temperature in the parametrization of SC potential, a_0 obtained for Q-SC is closer to experimental value.

3.1.3 Phonon Dispersion Relations

The force constants of Pd-Ni system are calculated by using the expression given in Eq. 2.34. We study the effective interaction range in order to demonstrate the sensitivity of the force constants on the cutoff. The force constants decay rapidly with distance and they are negligible beyond the eighth nearest neighbor shell. Table 3.2 shows the non-vanishing elements of the force constants for Pd, Ni and $Pd_{0.45}Ni_{0.55}$. Comparison with the force constants calculated through the neutron measurements [7] reveals good agreement.

Phonon dispersion curves for Pd at 120 K, Ni at 300 K and $Pd_{0.45}Ni_{0.55}$ at 300 K are presented in Figs. 3.2-3.4, respectively. The calculations are performed

Table 3.2: Force constants of Pd, Ni and $Pd_{0.45}Ni_{0.55}$ in the units of dyn/cm up to the 8^{th} nearest neighbor (NN) shell by using Q-SC potential parameters.

			Force Constants					
NN	Comp.		Pd		Ni		$Pd_{0.45}Ni_{0.55}$	
1	xx	zz	-16980	1532	-17447	1914	-18095	2776
	xy		18129		-19111		25300	
2	xx	yy	528	262	783	85	666	245
3	xx	yy	-265	34	-63	-37	-218	30
	yz	xz	139	-171	-24	-84	-112	-310
4	xx	zz	-200	-8	-113	-112	-192	12
	xy		202		-105		-194	
5	xx	yy	-44	7	-176	4	-34	4
	zz	xz	-44	21	-18	-11	5	16
6	xx	yy	-0.5	-10	-2.63	-6	-7	-14
7	xx	yy	-10	0.6	-8	0.3	-8	-3
	zz	yz	-4	3	-0.3	2	0.7	3
	xz	xy	7	-3	-5	2	2	-5
8	xx	yy	-6	0.7	-4	0.05	-10	1

by using both the SC parameters (dashed lines) and the Q-SC parameters (solid lines). The plots are shown along three principal symmetry directions, together with the experimental data [7, 79, 80]. While Q-SC potential improves the description of phonons for Ni and $Pd_{0.45}Ni_{0.55}$, it does not show any improvement on the phonon frequencies for Pd. Generally Q-SC calculations are in better agreement with experimental values. However, we may have to underline the fact that although SC potential has been fitted to only three experimental quantities, it still describes phonon properties well. The phonon spectra of $Pd_{0.45}Ni_{0.55}$ obtained from Q-SC is consistent with the experiment as shown in Fig. 3.4. This encourages us to study the phonon dispersion relations at other concentrations of the Pd-Ni system, which are not available in the literature. The results for the transverse (T) and longitudinal (L) phonon frequencies for Pd-Ni alloys at

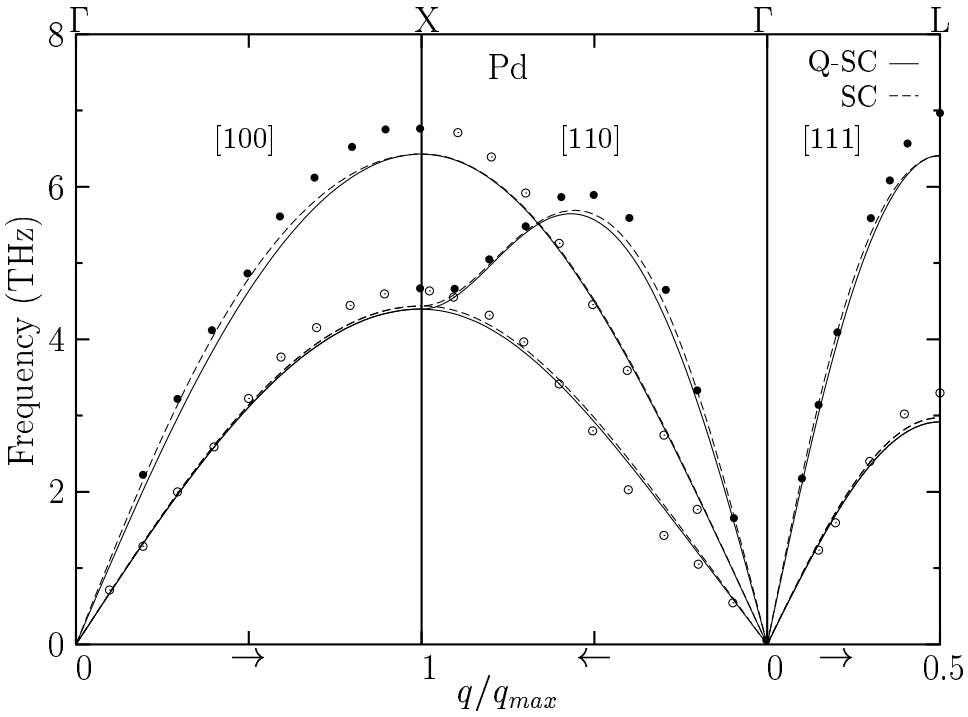

Figure 3.2: Phonon dispersion curves of Pd along symmetry directions. The solid curves represent the present calculations using Q-SC parameters. The dashed curves show the SC calculations. The points are the experimental data by Miller and Brockhouse [79] at 120 K.

X and L points at the Brillouin zone are given in Figs. 3.5. As the concentration of Pd increases in Ni, transverse frequencies decrease linearly (Figs. 3.5 (a) and (c). On the other hand, longitudinal frequencies show polynomial behavior as given in Figs. 3.5 (b) and (d). Calculation of the phonon dispersion curves as a function of temperature can be useful to identify unstable phonon modes. Hence, we are interested in variation of frequencies with temperature. The frequencies at various temperatures for Pd and Ni at the Brillouin zone are listed in Table 3.3. As expected, the frequency of phonons decreases with temperature.

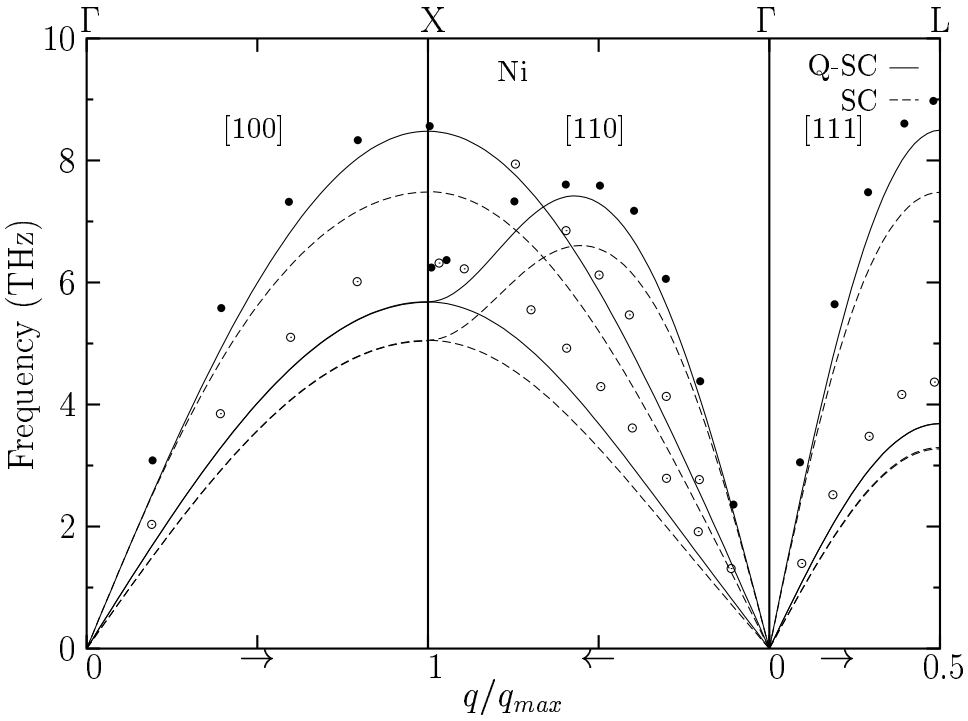

Figure 3.3: Phonon dispersion curves of Ni along symmetry directions. The points are the experimental data by Birgeneau *et al.* [80] at 300 K. The other symbols are the same as that of Fig.3.2.

Q-SC simulation results at 300 K are compared with experimental data [81] in the same table. Also included in Table 3.3 are the other simulation results. The Q-SC results are more compatible with the experimental values than the results of previous works using SM-TBM [82] and EAM [35] except for the transverse modes of Ni. The best agreement with the experiment is the longitudinal frequency at X point (ν_{XL}) for Ni, as expected, due to fitting of Q-SC parameters to experimental phonon frequencies at that point.

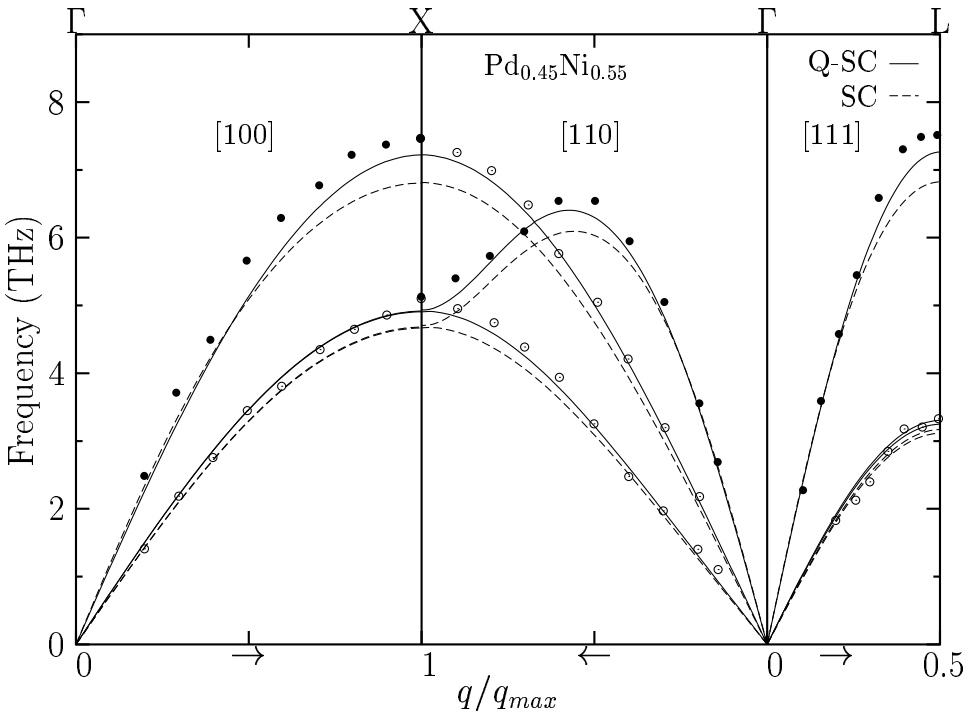

Figure 3.4: Phonon dispersion curves of $Pd_{0.45}Ni_{0.55}$ along symmetry directions. The points are the experimental data by Kamitakahara and Brockhouse [7] at 300 K. The other symbols are the same as that of Fig.3.2.

3.1.4 Elastic Constants

As a further test for the derived force constants, the elastic constants are calculated via the method of long waves which relates the elastic constants calculated by the slopes of the dispersion curves as k→0. However, this is a very delicate procedure since small errors in long range couplings strongly influence the result. Alternatively, the elastic constants can be derived via homogeneous deformation of unit cell from the second derivative of the total energy with respect to the deformation. The second direct approach is provided by using the statistical fluctuation formulae given in Ref. [72]. The elastic properties of bulk

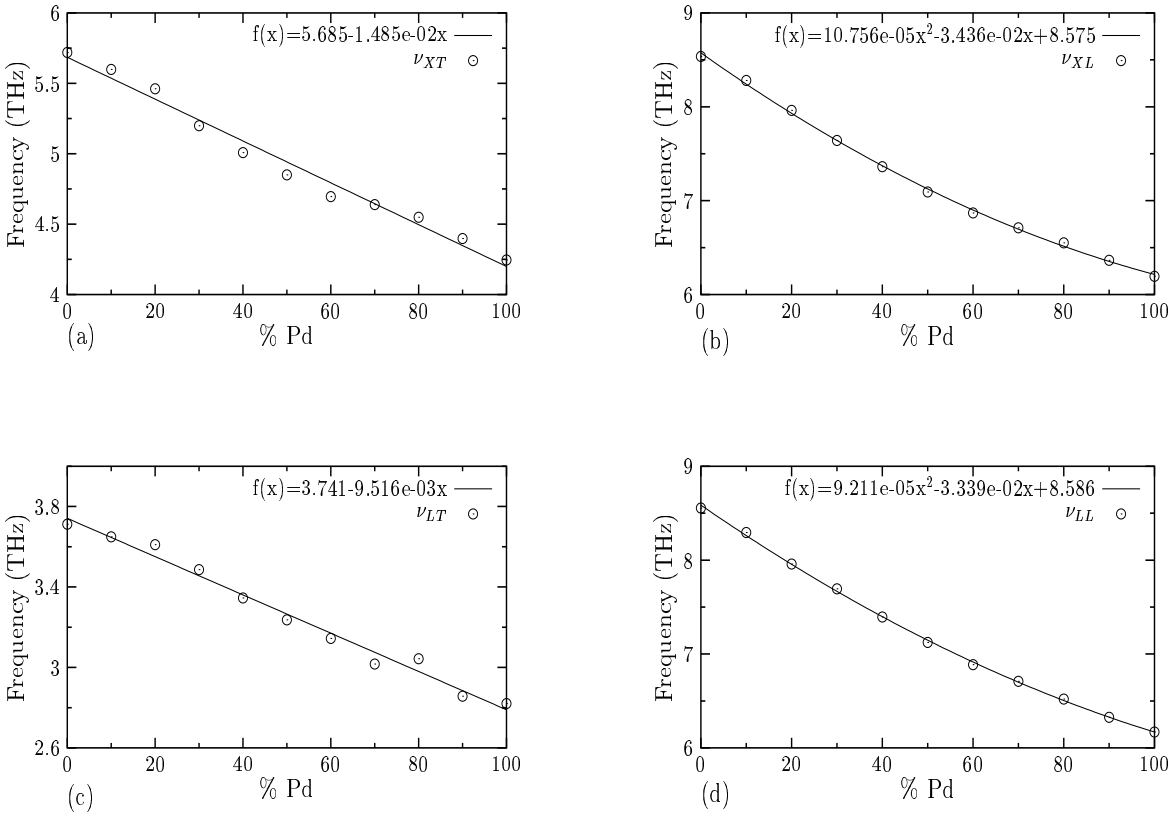

Figure 3.5: The phonon frequencies for (a) the transverse branches at the X point (ν_{XT}), (b) the longitudinal branch at the X point (ν_{XL}), (c) the transverse branches at the L point (ν_{LT}), (d) the longitudinal branch at the L point (ν_{LL}) at the Brillouin zone as a function of concentration of Pd in Ni at 300 K. The points are simulation results. Our data are fitted to the functions given in the figures.

Pd-Ni alloys are calculated by using both SC and Q-SC parameters over 50000 steps in the EVN, hence resulting in the adiabatic elastic constants. Table 3.4 compares our results for the elastic constants at 300 K as obtained with two methods with the experimental values [83]. A reasonable consistency of both sets of elastic constants for two potentials are achieved, except for elastic constant C_{44} for Ni (the discrepancy is about 19 %). The values for Ni derived from the

Table 3.3: Comparison of the calculated and experimental transverse (T) and longitudinal (L) phonon frequencies at the Brillouin zone boundaries X and L for Pd and Ni. The first row is the calculations using Q-SC at various temperatures. The experimental (Exp) [81] and other simulation results at 300 K are given in the second row. Our results compared with the other two potential methods: embedded atom model (EAM) [35] and second-moment tight binding method (SM-TBM) [82].

Metal	Model	T (K)	ν_{XT} (THz)	ν_{XL} (THz)	ν_{LT} (THz)	ν_{LL} (THz)
Pd	Q-SC	300	4.25	6.19	2.83	6.17
		500	4.08	5.93	2.73	5.90
		700	3.93	5.68	2.60	5.62
		900	2.64	3.89	2.49	5.30
	Exp	300	4.56	6.70	3.21	6.86
	SM-TBA	300	4.02	5.77	2.67	5.72
	EAM	300	5.91	4.09	2.66	5.88
Ni	Q-SC	300	5.68	8.48	3.69	8.50
		500	5.52	8.20	3.58	8.21
		700	5.33	7.90	3.46	7.90
		900	5.11	7.58	3.36	7.55
	Exp	300	6.17	8.55	4.24	8.88
	SM-TBM	300	6.78	9.88	4.49	9.80
	EAM	300	6.78	9.90	4.52	9.77

long waves method are in more reasonable agreement with experiment than those based on homogeneous deformation method, as shown in Table 3.4. This is due to the consistency of phonon dispersion curves with the experiment.

The results obtained from the homogeneous deformation method for pure metals at 0 K and alloys at 300 K are given in Table 3.5, along with comparison with experimental data, where available, and the results of previous works using different potential models. As shown, the potential used by Cleri and Rosato [82] for the elastic constants is yielding better results. The elastic constants and bulk modulus both from Q-SC and SC calculations agree with the available experiment and the other calculations except for elastic constant C_{44}. The only

Table 3.4: Elastic constants of Pd and Ni at 300 K in the units of GPa. The calculated results (with Q-SC and SC) are obtained by homogeneous deformations (H) and long waves (L) methods. Experimental values are taken from Ref. [83]

Metal	Els. Cons.	Exp	Q-SC			SC		
			H	L	ΔHL(%)	H	L	ΔHL(%)
Pd	C_{11}	227.1	201.89	186.71	-7.1	229.48	214.21	-6.7
	C_{12}	176.0	140.15	125.67	-10.3	164.45	149.74	-8.9
	C_{44}	71.7	81.44	79.78	-2.0	82.72	81.29	-1.7
Ni	C_{11}	250.8	214.57	237.42	10.7	213.69	237.55	11.2
	C_{12}	150.0	152.95	164.53	7.6	166.10	180.34	8.6
	C_{44}	123.5	89.04	105.93	19.0	69.91	83.36	19.2

metal alloy studied here for which the first-principle calculations are available is Pd. The accuracy of the Q-SC elastic constant C_{11} for Pd, showing a deviation of 8 % from experiment, is comparible to that of the EAM [84] and the first-principle calculations [85], while SC elastic constant C_{12} is in good agreement with experiment. The experimental data on the elastic constants for Pd-Ni alloys are not available for comparison. Our results for $Pd_{0.45}Ni_{0.55}$ are smaller than the values calculated by Upadhyaya *et al.* [8] using the TMMP of Animalu [10] except for C_{12} calculated from SC. We are also interested in temperature dependence of elastic constants in order to see whether there is an improvement of using Q-SC on the results. As the temperature increases, the Q-SC parameters improve the elastic constants slightly, as shown in Table 3.6. Thermal softening of the alloy occurs with increasing temperature.

Table 3.5: Comparison of calculated and experimental (Exp) [83] values for elastic constants C_{ij} and bulk modulus B at 0 K for pure metals and at 300 K for Pd-Ni alloys in the units of GPa. Our results (Q-SC and SC) for Pd and Ni are compared with the other potential models: embedded atom method (EAM) [84], second moment tight binding method (SM-TBM) [82], first-principles full potential (LAPW) [85], where available. A comparison for $Pd_{0.45}Ni_{0.55}$ is made between our results of Q-SC and SC calculations and transition metal model potential (TMMP) [8].

Metal	Model	C_{11}	C_{12}	C_{44}	B
	Exp	234.12	176.14	71.17	195.00
	Q-SC	216.00	150.25	91.66	172.17
Pd	SC	248.20	175.90	93.29	200.00
	EAM	218.00	184.00	65.00	195.00
	SM-TBM	232.00	178.00	73.00	196.00
	LAPW	218.00	172.00	74.00	
$Pd_{0.8}Ni_{0.2}$	Q-SC	198.83	145.69	79.37	163.02
$Pd_{0.6}Ni_{0.4}$	Q-SC	197.63	150.64	77.83	165.75
$Pd_{0.45}Ni_{0.55}$	Q-SC	199.13	153.29	77.69	168.57
	SC	214.97	174.33	69.34	187.88
	TMMP	224.50	154.70	94.50	
$Pd_{0.4}Ni_{0.6}$	Q-SC	199.28	152.54	78.20	168.00
$Pd_{0.2}Ni_{0.8}$	Q-SC	204.81	154.37	82.26	170.78
	Exp	261.20	150.80	131.70	188.00
	Q-SC	219.59	165.34	99.57	183.62
Ni	SC	226.61	178.77	79.24	194.73
	EAM	233.00	154.00	128.00	180.40
	SM-TBM	257.00	155.00	136.00	189.00

Table 3.6: Comparison of calculated (Q-SC and SC) and experimental (Exp) [83] values for elastic constants C_{ij} of Ni at various temperatures.

	Exp			Q-SC			SC		
T (K)	C_{11}	C_{12}	C_{44}	C_{11}	C_{12}	C_{44}	C_{11}	C_{12}	C_{44}
0	261.20	150.80	131.70	216.33	165.337	99.39	251.736	191.12	89.44
300	250.80	150.00	123.50	214.57	152.95	89.04	213.69	166.10	69.91
500	239.60	149.00	115.90	203.87	147.53	82.79	201.73	158.84	63.58
700	226.10	147.30	107.90	193.34	141.75	76.35	188.20	151.21	56.65

3.2.1 Melting Temperature

The melting temperatures (T_m) of Pd-Ni alloys are determined by examining the behavior of density, enthalpy, and pair distribution function as a function of temperature. To better describe the melting points, we also check the diffusion coefficients of Pd-Ni alloys. We obtain the same melting temperatures from all these physical properties. T_m of Pd-Ni alloys are plotted in Fig. 3.6, along with experimental results [18]. The melting points of pure Pd (1820 K $\pm$ 10 K) and pure Ni (1710 K $\pm$ 10 K) metals are in very good agreement with experimental values, as shown in the figure. As we go into the alloy, this accuracy decreases with the maximum deviation of 5.3 %. This is due to the potential parameters of binary metal alloys calculated by using those of pure metals using the combination rules. Our results follow the trend of the experiments. The calculated values are slightly lower than the experimental ones. We find eutectic region between concentrations around $Pd_{0.5}Ni_{0.5}$ and $Pd_{0.3}Ni_{0.7}$, supporting the critical experimental concentration of $Pd_{0.45}Ni_{0.55}$. The region over the data points shows the alloy in liquid phase and the region below the points gives the alloy in solid phase. We have also obtained the melting temperatures of pure Pd and pure Ni metals by using SC potential parameters. The melting points of Pd and Ni are found to be 1760$\pm$10 K (65 K lower than experimental value) and 1420$\pm$10 K (306 K lower than experimental value), respectively. Since Q-SC potential parameters are working better in predicting the melting temperatures of Pd-Ni alloys, we

present the results obtained from Q-SC parameters from now on.

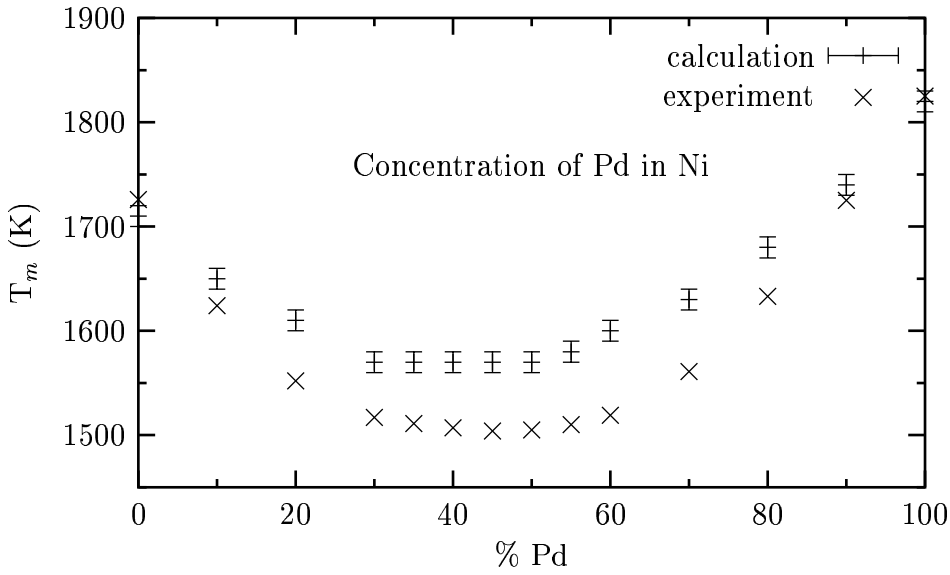

Figure 3.6: The melting temperatures T_m of Pd-Ni alloys as a function of Pd concentration in Ni. The experimental points are from Ref. [18].

3.2.2 Density and Enthalpy

The temperature dependence of density and enthalpy of Pd, Ni and $Pd_{0.4}Ni_{0.6}$ are shown in Fig. 3.7 (a) and (b), respectively. The discontinuity in the figures shows the structural transformation from solid phase to liquid phase. The T_m is identified by monitoring the jump in the figures. At T_m, we find the density for Pd and Ni to be 10.53 and 7.94 g/cm^3, respectively. These values are consistent with experimental values which are 10.49 and 7.90 g/cm^3, respectively [20].

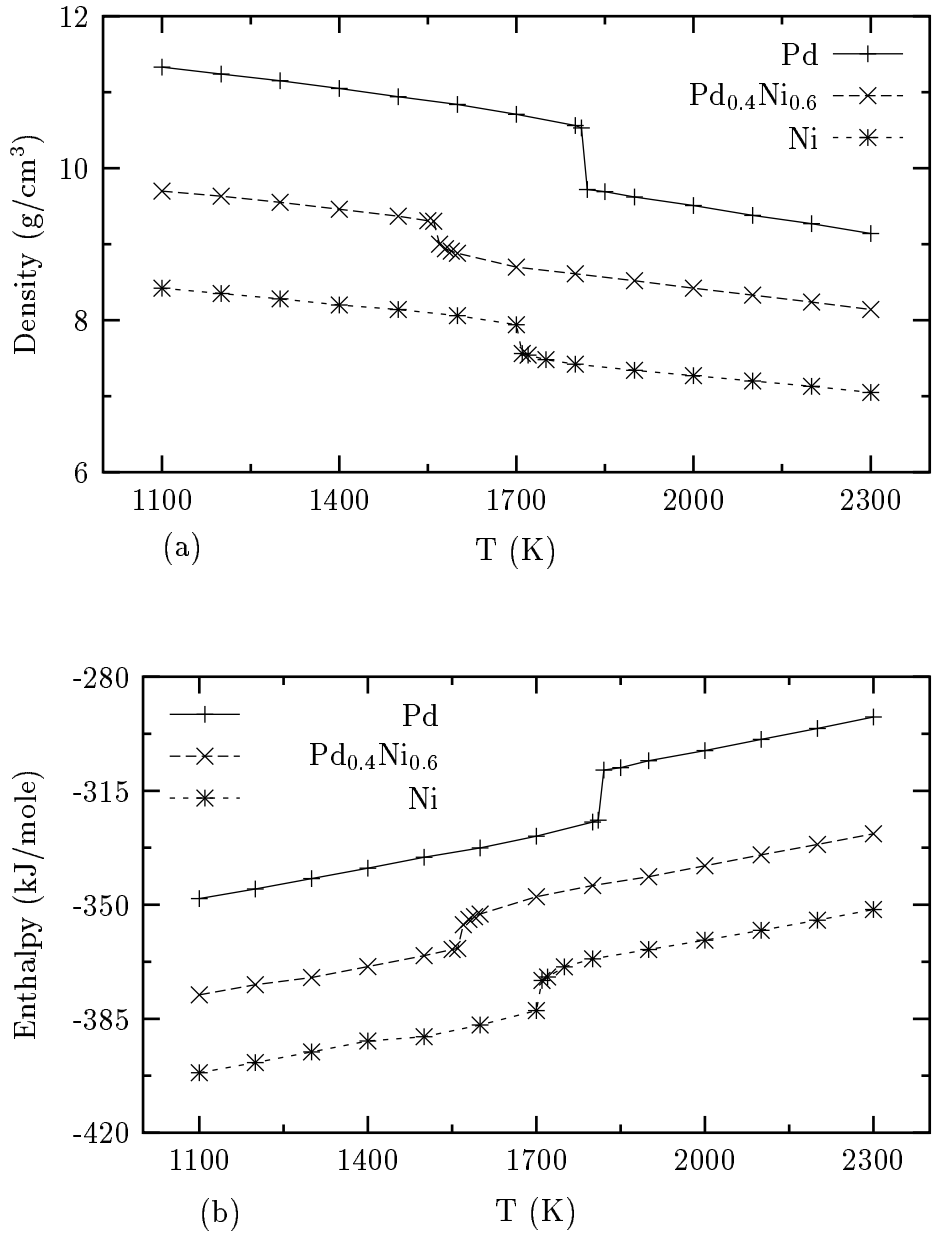

Figure 3.7: (a) Density and (b) enthalpy of Pd, Ni, and $Pd_{0.4}Ni_{0.6}$ as a function of temperature.

3.2.3 Pair Distribution Function and Static Structure Factor

Our results for the pair distribution function g(r) are presented in Fig. 3.8 for Pd, Ni and $Pd_{0.45}Ni_{0.55}$ alloy. Fig. 3.8 (a) shows g(r) computed for Pd at 1853 K and Ni at 1873 K. The position of the first peak compares well with the experimental results; for Ni, it is the same as Waseda's results [86] which is 2.40 A^0, while for Pd it is 2.67 A^0 and experimental result is 2.60 A^0.

The path we follow to predict the T_m from g(r) may be seen in Fig. 3.8 (b) plotted at selected temperatures; 1600 K, 1810 K, 1820 K and 2000 K for Pd. The metal shows the structure with the peaks at solid or near some of the ideal fcc atomic positions at 1600 K and 1810 K. The peaks are broadened and lowered at 1820 K. Some peaks disappear, indicating that the liquid dynamics is activated. After this temperature, the metal goes into the liquid state (2000 K).

Partial pair distribution functions $g_{\alpha\beta}(r)$ for $Pd_{0.45}Ni_{0.55}$ at 1800 K are given in Fig. 3.8 (c). The first peak in the g_{Pd-Ni}(r) curve lies midway between the first peaks in the g_{Pd-Pd}(r) and g_{Ni-Ni}(r) curves. We have also studied concentration effect on $g_{\alpha\beta}(r)$ at the same temperature. It is observed that Ni causes to reduce the height of the first peaks in Pd-Pd and Ni-Ni pairs and does not affect that of Pd-Ni pairs. The height of total g(r) decreases up to the concentration around 60 % of Pd. Also the slight shift towards to left is observed in the total g(r) as the concentration of Ni in Pd increases, while not in $g_{\alpha\beta}(r)$. In the other peaks, shift is shown, while their heights does not change.

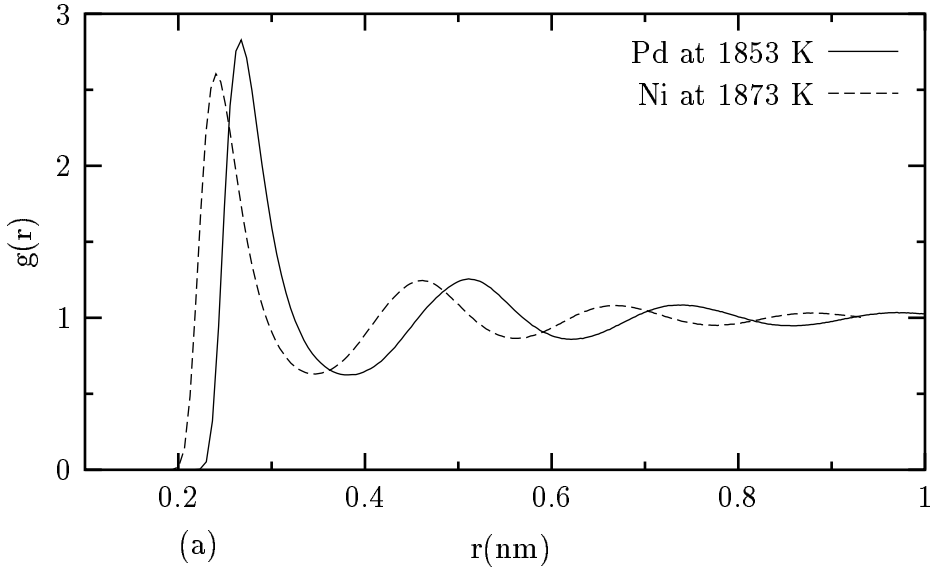

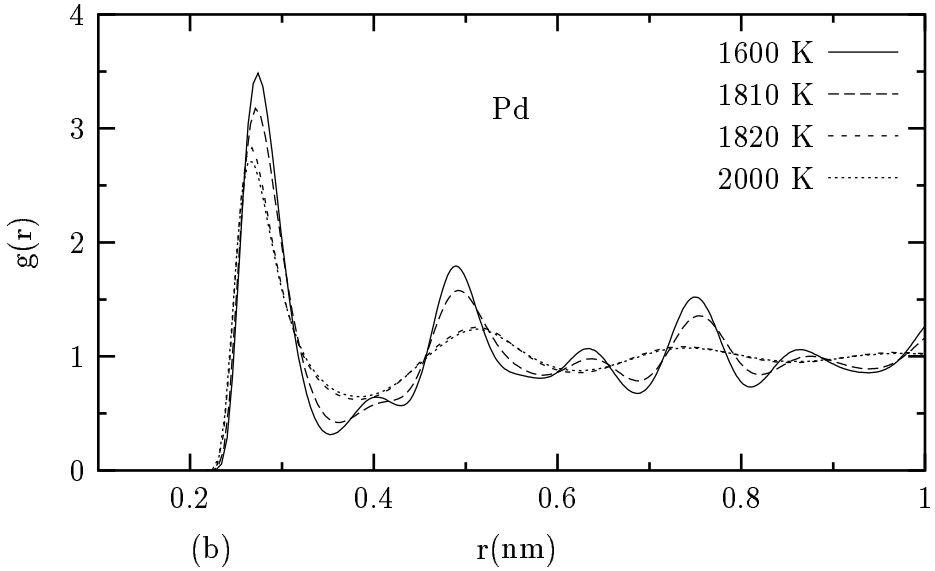

Figure 3.8: Pair distribution function g(r) (a) for Pd at 1853 K and Ni at 1873 K, (b) for Pd at various temperatures. (c) Partial pair distribution function $g_{\alpha\beta}(r)$ for $Pd_{0.45}Ni_{0.55}$ at 1800 K.

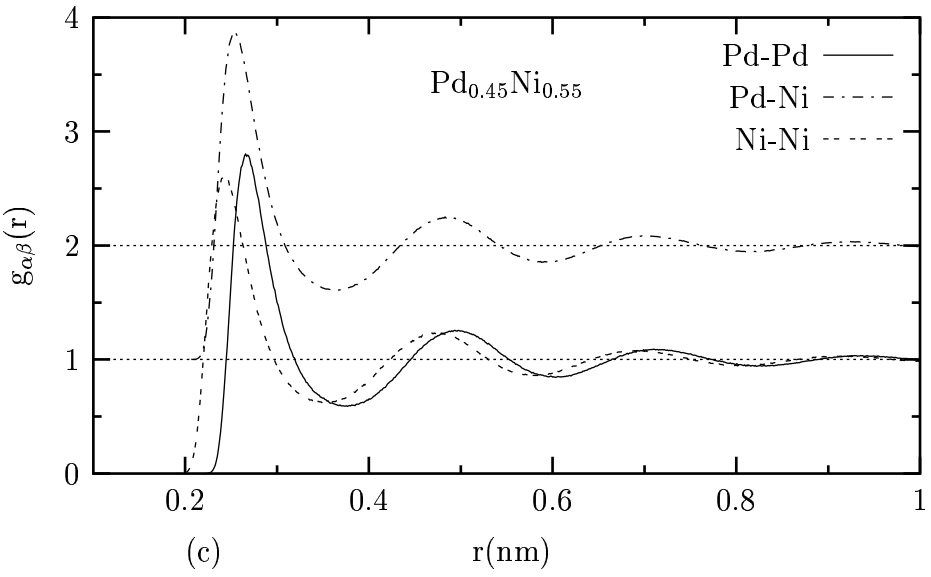

Figure 3.8: (continued).

The static structure factor, Fourier transform of g(r), gives the experimentally measurable structural information [54]. The simulation results for the static structure factor for Ni and Pd are shown in Fig. 3.9 (a) and Fig. 3.9 (b), respectively, along with the x-ray scattering experiments taken from Waseda [86]. The height of main S(q) peak of Ni is in agreement with the experiment, while the position of the first peak appears to be slightly shifted from the experimental data. Our result of Ni is also comparable with that of MEAM [16]. On the other hand, the EAM [87, 88, 89] underestimates the height of main S(q) peak of Ni and leads to the discrepancy with Waseda's results. Foiles [87] and Holzman *et al.* [88] attributed discrepancy with Waseda's x ray data to the method which was not convenient for Ni or to the potential parameters that they used, while Alemany *et al.* [89, 90] reported that there was a systematic error in the method

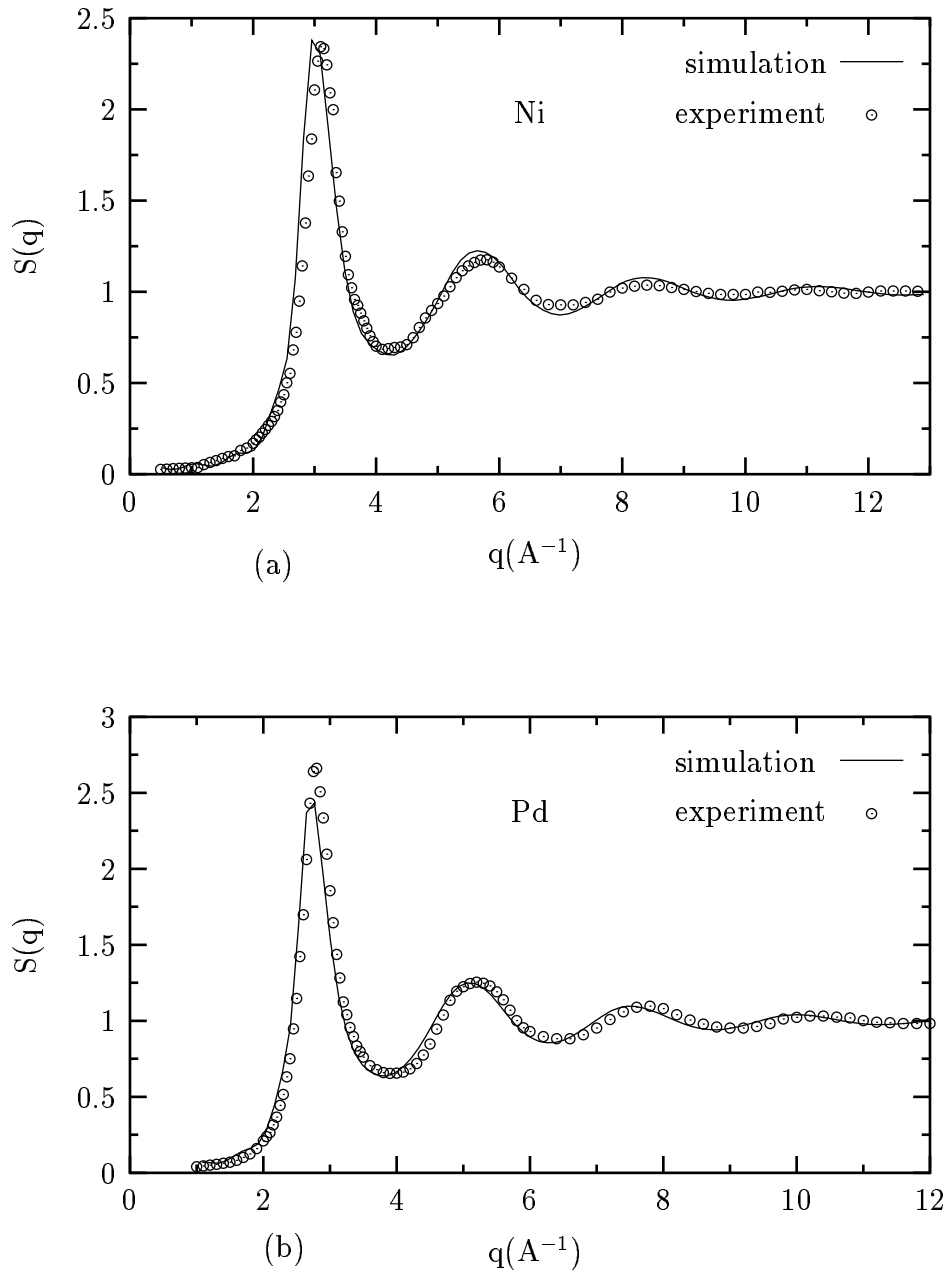

Figure 3.9: Static structure factor S(q) for (a) liquid Ni at 1873 K and (b) liquid Pd at 1853 K. The solid line is the simulation results and the points are the experimental data [86].

used by Waseda. As far as Pd is concerned, main peak is lower than experimental data, whereas the position of first peak agrees well with the experiment. These problems may be inherent in any parametrization based only on solid state data.

3.2.4 Diffusion Coefficients

We have obtained the T_m by also checking the diffusion coefficients. The diffusivities of the order of 10^{-3} nm^2ps^{-1} helps us to distinguish the liquid state from the solid state [20]. The velocity auto-correlation function (VAC) and mean square displacement (MSD) are used to compute the diffusion coefficients. The normalized VAC for Pd at various temperatures is illustrated in Fig. 3.10. Atoms at low temperatures remember the initial velocities more than those at high temperatures, as shown in the figure. It is known that the center atom is surrounded

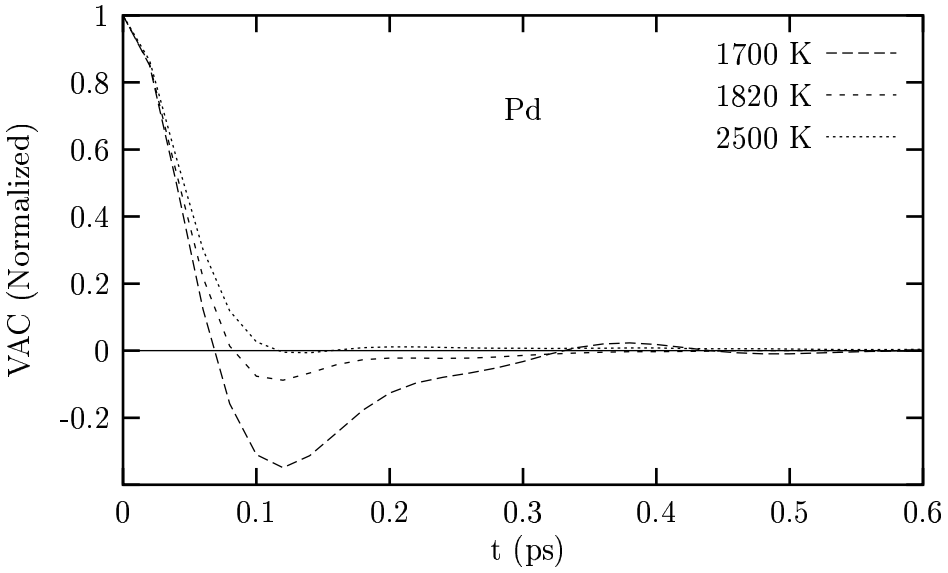

Figure 3.10: Normalized velocity auto-correlation function $C_v(t)$ of Pd at different temperatures.

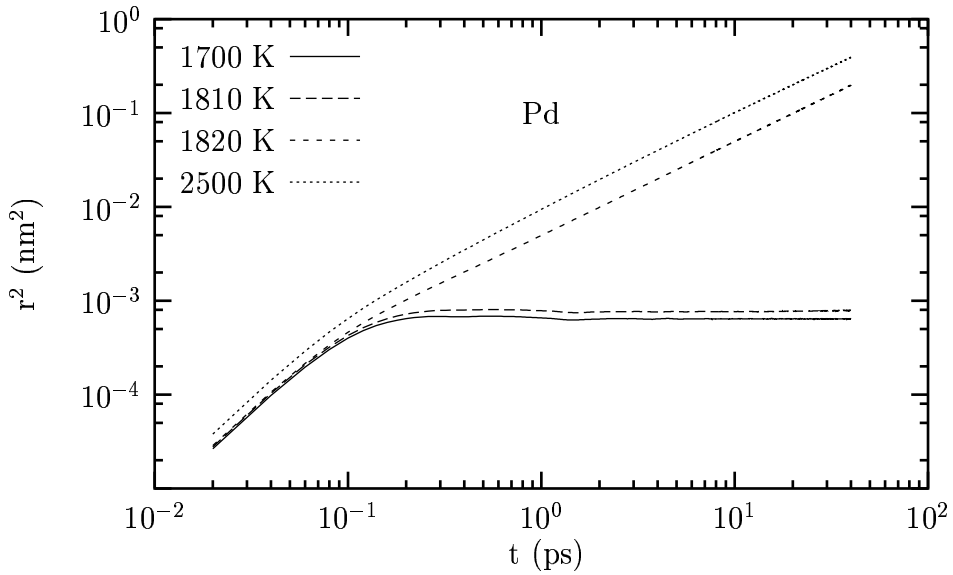

Figure 3.11: Mean square displacement $r^2(t)$ of Pd at various temperatures.

by a cage of nearest-neighbor atoms and the cage wall cause atoms to loose memory of the initial velocities. Atoms are closely packed in the solid phase (1700 K), such that they prefer reflecting from this wall instead of diffusing, which represents the trend of negative slope. Then, atoms redevelop the memory of the momentum, in which the positive slope of VAC occurs. VAC becomes negative and takes a minimum value before reaching zero at liquid densities (1820 K). In dense fluid (2500 K), VAC remains positive and decays exponentially to zero [91]. The time dependent position of the particles computed from Eq. 2.44 is shown in Fig. 3.11. The MSD shows a quadratic dependence at short times in the liquid phase, as seen in the figure. On the other hand, at longer times, the linear dependence of the MSD plot is apparent, which shows the diffusive motion. For solid phase, the situation at short times is similar to the one in the liquid phase.

The atoms are trapped in the cage at longer times, showing a plateau behavior. As seen in the figure, the T_m for Pd is obvious (1820 K).

We now present our results for the self-diffusion coefficient. First, we analyze the diffusion coefficients as a function of temperature. Second, we compare them with the experimental data and other calculations, where available. The diffusion coefficients of Pd-Ni alloys are computed from GK (Eq. 2.41) and E (Eq. 2.43) relations. The temperature dependence of our diffusion coefficient data exhibits the Arrhenius-type behavior;

$$D(T) = D_0 exp(-E_a/k_B T) \quad , \tag{3.1}$$

where D_0 is the self-diffusion prefactor and E_a is the diffusional activation energy. The values for Arrhenius diffusion parameters are given in Table 3.7. D_0 and E_a of Ni are comparable in values of 108.0 nm^2/ns and 0.476 eV, respectively, with

Table 3.7: Arrhenius equation parameters for self-diffusion and shear viscosity values computed by fitting to the MD simulation results of self-diffusion from the Einstein (E) relation and viscosity from the Green-Kubo (GK) relation. The units of D_0, η_0, and E_a and E_{vis} are in nm^2/ns, mPa.s, and eV, respectively.

	Diffusion				Viscosity	
	Pd		Ni			
	D_0	E_a	D_0	E_a	η_0	E_{vis}
Pd	89.40	0.461	-	-	0.479	0.288
$Pd_{0.8}Ni_{0.2}$	113.69	0.514	117.733	0.488	0.429	0.314
$Pd_{0.6}Ni_{0.4}$	90.064	0.466	108.818	0.466	0.444	0.304
$Pd_{0.4}Ni_{0.6}$	87.036	0.459	101.514	0.455	0.595	0.239
$Pd_{0.2}Ni_{0.8}$	87.710	0.454	99.705	0.446	0.578	0.232
Ni	-	-	103.260	0.449	0.624	0.213

Cai-Ye embedded atom method (CY-EAM) used by Cherne and Baskes [16]. However, E_a predicted by Protopapas *et al.* [19] is higher by a factor greater than 2 with our results for Ni. Logarithmic presentation displayed in the Arrhenius-type diagram, with D as a function of 1000/T for Pd, Ni and $Pd_{0.6}Ni_{0.4}$ are given in Fig. 3.12. The solid line in the first two figures represents an Arrhenius best fit for curve through data points evaluated from GK relation. Dashed line corresponds to fit for E. As shown in the figures, the values of D computed by using the GK and E relations are mutually consistent. The data in the figures fit well to Eq. 3.1. The Arrhenius curve of E for $Pd_{0.6}Ni_{0.4}$ is illustrated in Fig. 3.12 (c). As we see in this figure that D of Ni is larger than that of Pd because the atomic size of Ni is smaller than that of Pd. Table 3.8 lists the computed values of D fitted to Arrhenius equation for Pd and Ni along with the available experimental data [19] and the other simulation results. Also included in Table 3.8 are the D computed from E relation for Pd-Ni alloys. The only metal alloy studied here for which the experimental values of D are available is Ni [19]. Our simulation results for Ni are consistent with the experimental values. This value is also more compatible with the value predicted by Yokoyama [92] using a hard sphere (HS) description than the previous works using SM-TBM [90] and EAM [89, 93]. Our results for D of Pd at 1853 K agree with the values calculated by the previous works reported in Refs. [90, 93, 94]. There are no experimental and theoretical results for Pd-Ni alloys to compare with our simulations. Self-diffusion coefficients of Pd and Ni increases with increasing concentration of Ni in Pd-Ni alloys, as seen in Table 3.8. This value does not change significantly around

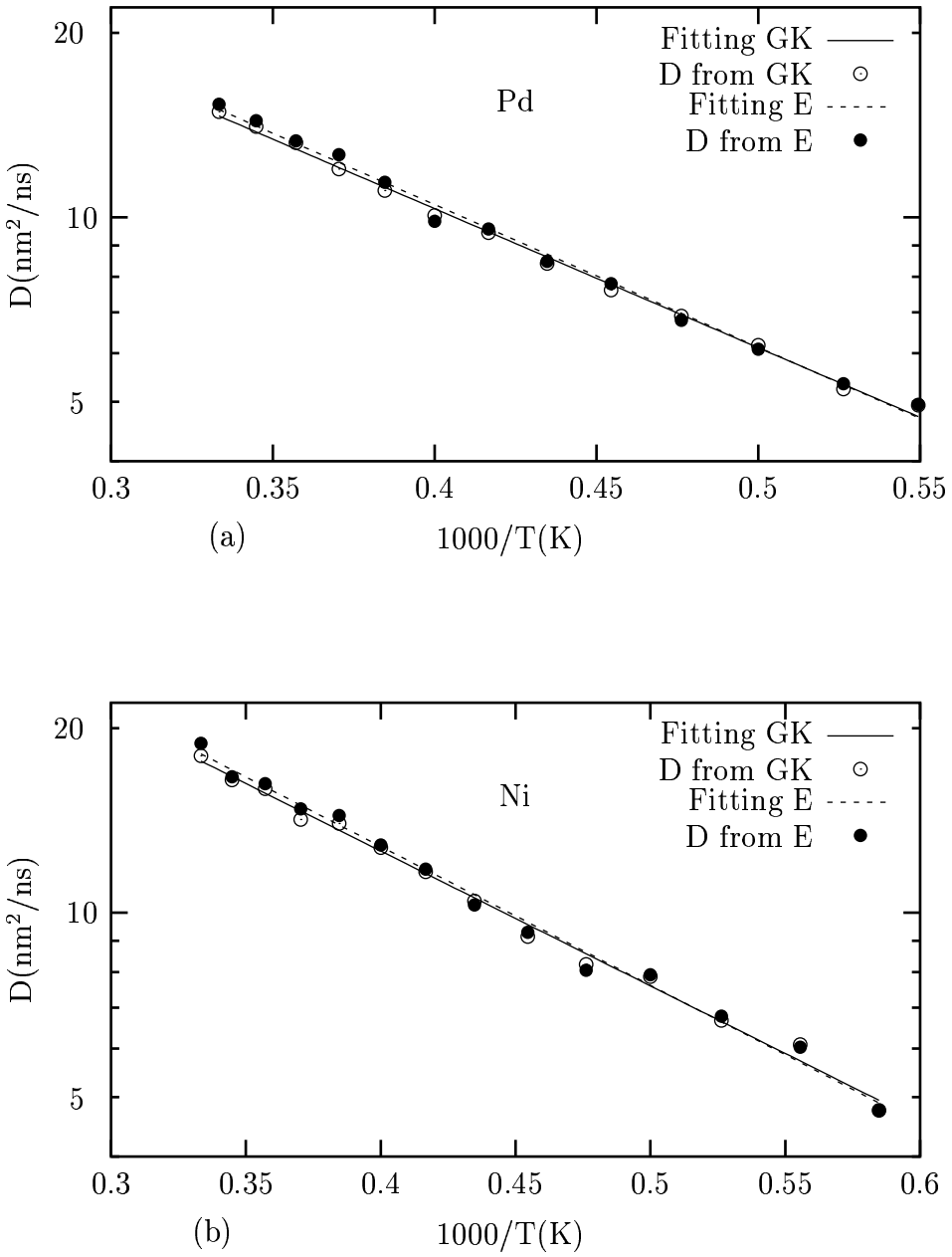

Figure 3.12: Arrhenius plot of diffusion coefficients D computed from (a) Green-Kubo (GK) and Einstein (E) relations for Pd, (b) GK and E relations for Ni, and (c) E relation for $Pd_{0.6}Ni_{0.4}$.

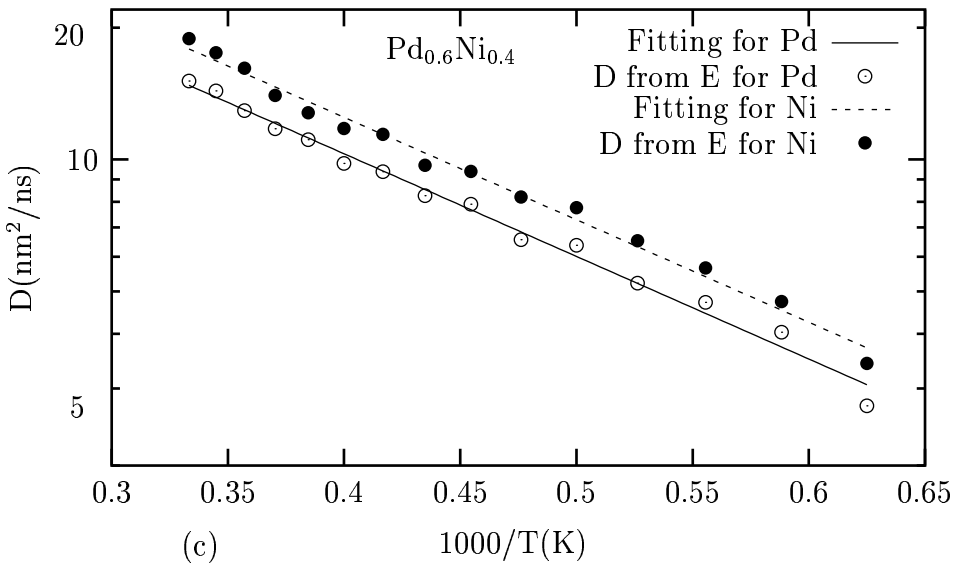

Figure 3.12: (continued).

the eutectic region. This event could be also seen in the time dependence on the neighbor list correlation function $C_\ell(t)$, the measurement of the change in the nearest neighbor numbers during the simulation time [76]. Fig. 3.13 illustrates the normalized $C_\ell(t)$ as a function of time for different concentrations of Pd-Ni alloys at 1800 K. Atoms at the concentration of $Pd_{0.8}Ni_{0.2}$ are less diffusive than that of $Pd_{0.2}Ni_{0.8}$, as shown in the figure. That is, as the concentration of Ni increases in Pd-Ni alloys, pair atoms survive less in a chosen cut-off distance.

3.2.5 Viscosity

We have also studied the viscosity of the Pd-Ni metal alloys as a liquid property. Our results obey an Arrhenius relationship over the temperature range we have studied;

Table 3.8: Diffusion coefficients D in nm^2 ns^{-1} as evaluated by using the Green-Kubo (GK) and Einstein (E) relations at the shown temperatures for pure Pd, Ni and their binary alloys. Here calculated diffusion coefficients are obtained from Arrhenius equation. HS denotes hard sphere model used in Ref. [92]. Experimental data are taken from Ref. [19]

		D(nm^2 ns^{-1})			
Metal	T(K)	Simulation	Exp.	Other Calculations	Ref.
Pd	1853	4.98 (GK) 4.96 (E)		3.80 (GK) 3.83 (E)	[94]
				4.03 (GK) 4.07 (E)	[90]
	near melting			4.49 (E)	[93]
Ni	1773	5.48 (GK) 5.45 (E)	4.61	2.52 (GK) 2.54(E)	[90]
				3.52 (GK) 3.56 (E)	[89]
				4.49 (HS)	[92]
	near melting			3.85 (E)	[93]
	1873	6.39 (GK) 6.38 (E)	5.96	4.31 (GK) 4.34 (E)	[89]
				5.60 (HS)	[92]
		Self-diffusion coefficients from E			
		Pd	Ni		
$Pd_{0.8}Ni_{0.2}$	1873	4.70	5.73		
$Pd_{0.6}Ni_{0.4}$	1873	5.00	6.07		
$Pd_{0.4}Ni_{0.6}$	1873	5.08	6.05		
$Pd_{0.2}Ni_{0.8}$	1873	5.22	6.29		

$$\eta(T) = \eta_0 exp(E_{vis}/k_B T) \quad , \tag{3.2}$$

where values for the parameters η_0 and E_{vis} are tabulated in Table 3.7. The activation energy for viscosity E_{vis} of Ni is in agreement with the results of Cherne and Baskes [16], while it is lower than the experimental range of 0.311-0.374 eV [20]. We report the viscosity results compared to the experimental data and other calculations, where available, in Table 3.9. The calculated viscosity of Ni is lower than the experimental data [95] and other calculations obtained by Yokoyama and Arai [96] by up to a factor of 2.0. But temperature variation is similar to that of

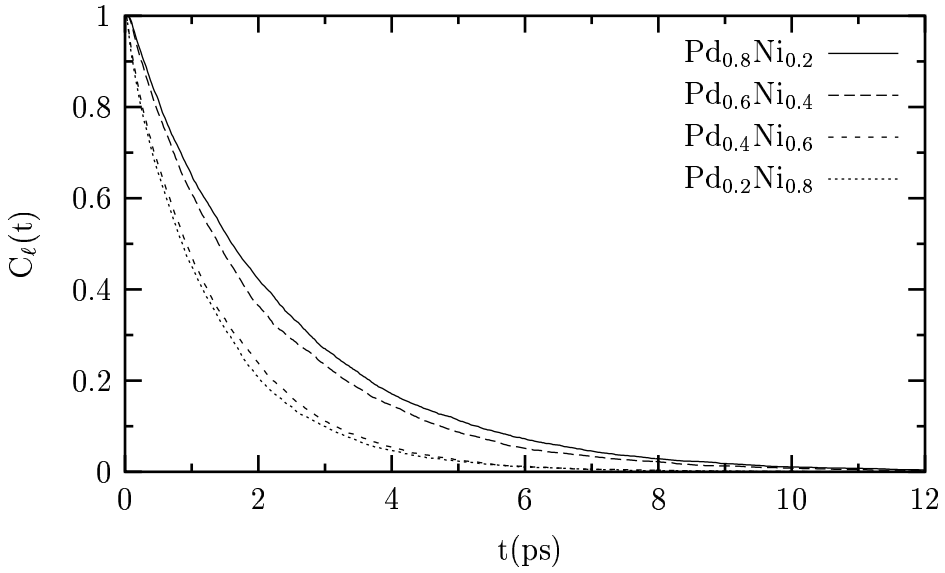

Figure 3.13: Neighbor list correlation function $C_\ell(t)$ for Pd-Ni metal alloys at 1800 K.

experiment. The experimental values have the errors of ± 1 % to ± 20 % [20], as has also been pointed out in the study of viscosity for Pu [97]. Hence this fact may explain the difference between the calculated and experimental viscosities. In addition, experimental viscosity values for liquid Ni at melting temperature vary from 4.5 mPa.s to 6.4 mPa.s [20]. There are also vast differences in the values of viscosity for Ni calculated by using other potential models [16, 90]. Our result for Pd whose experimental values are nonexistent is consistent with the viscosity calculated by using the SM-TBM [90]. Concentration dependence on viscosity at 1873 K is also given in Table 3.9. Decreasing in the viscosity with increasing Ni in Pd-Ni alloy is observed.

Table 3.9: Values of shear viscosity η of pure Pd, Ni and their binary alloys, as computed using the Green-Kubo (GK) relation at shown temperatures. Here calculated shear viscosities are obtained from Arrhenius equation. Experimental data are taken from Ref. [95].

		η (mPa.s)			
Metal	T(K)	Simulation	Exp.	Other Calculations	Ref.
Pd	1853	2.91		3.68	[90]
Ni	1773	2.50	4.8	5.76	[90]
				4.06	[96]
	1873	2.33	4.2	3.92	[96]
	1923	2.24	4.0	2.60	[96]
$Pd_{0.8}Ni_{0.2}$	1873	3.06			
$Pd_{0.6}Ni_{0.4}$	1873	2.98			
$Pd_{0.4}Ni_{0.6}$	1873	2.66			
$Pd_{0.2}Ni_{0.8}$	1873	2.48			

The atomic size ratio of Pd and Ni (r_{Pd}-r_{Ni}/r_{Ni}) is 0.11, leading to be a good candidate for forming metallic glass. In the Pd-Ni alloy system, eutectic point exists at 45 % of Pd. Hence, we select $Pd_{0.45}Ni_{0.55}$ as the metallic glass former.

3.3.1 Volume and Enthalpy

Figure 3.14 shows the volume and enthalpy of $Pd_{0.45}Ni_{0.55}$ as a function of the temperature in the heating and cooling processes. The cooling rates of 5×10^{12} K/s, 5×10^{11} K/s and 5×10^{10} K/s corresponding to the fast, intermediate, and slow cooling rates are used, respectively. A sudden increase in volume and enthalpy in the temperature range of 1500 K to 1600 K for the heating process is due to the melting of the Pd-Ni alloy. The calculated melting temperature T_m=1570 K is in good agreement with experimental melting temperature T_m=1504 K.

The curves of volume and enthalpy change linearly and are close to each other for all three cooling rates in the high-temperature region (3000 K-melting temperature). This indicates that the atoms move rapidly enough that they can reach easily to the speed with which the temperature is changed. In the intermediate temperature region ($T_m\approx$900 K), the slopes of the curves change slightly or have a noticeable bend. Liquid in this region is called a supercooled liquid. The relaxation times of the atoms are compatible with the time determined by the cooling rate. The atoms in liquid move slower under the fast and intermediate cooling conditions (5×10^{12} K/s and 5×10^{11} K/s), because the viscosity of the liquid

increases continuously as a supercooled liquid is cooled to lower temperatures. The relaxation times for molecular rearrangements exceed the time scale of the cooling process. Then the system is out of equilibrium at the temperature where the slopes of the curves of volume and enthalpy change. This temperature can be identified with the glass transition temperature T_g. Finally, atomic motion is frozen on the time scale of the experimental observations and non-crystalline solid, a glass forms. T_g can be defined in many different ways. It can be observed as discontinuities in thermal expansion, compressibility, or heat capacity versus temperature curves. T_g is the intersection of two lines with different slopes according to the Abraham's suggestion [98].

To contrast with the glass-transition observed in the Pd-Ni system at fast and intermediate cooling rates, we also consider the slow cooling rate (5×10^{10} K/s) to simulate the cooling process to examine the nature of the crystallization process. The volume and enthalpy curves in Figure 3.14 exhibit a pronounced discontinuity as the temperature is lowered below $\approx$900 K, which shows that a first-order phase transition occurs. At this rate, the atoms have enough time to move to their particular neighbor positions and crystallization occurs. In summary, Fig. 3.14 illustrates that we can obtain the glass formation at the cooling rate of 5×10^{12} K/s and 5×10^{11} K/s, and the crystallization at the cooling rate of 5×10^{10} K/s.

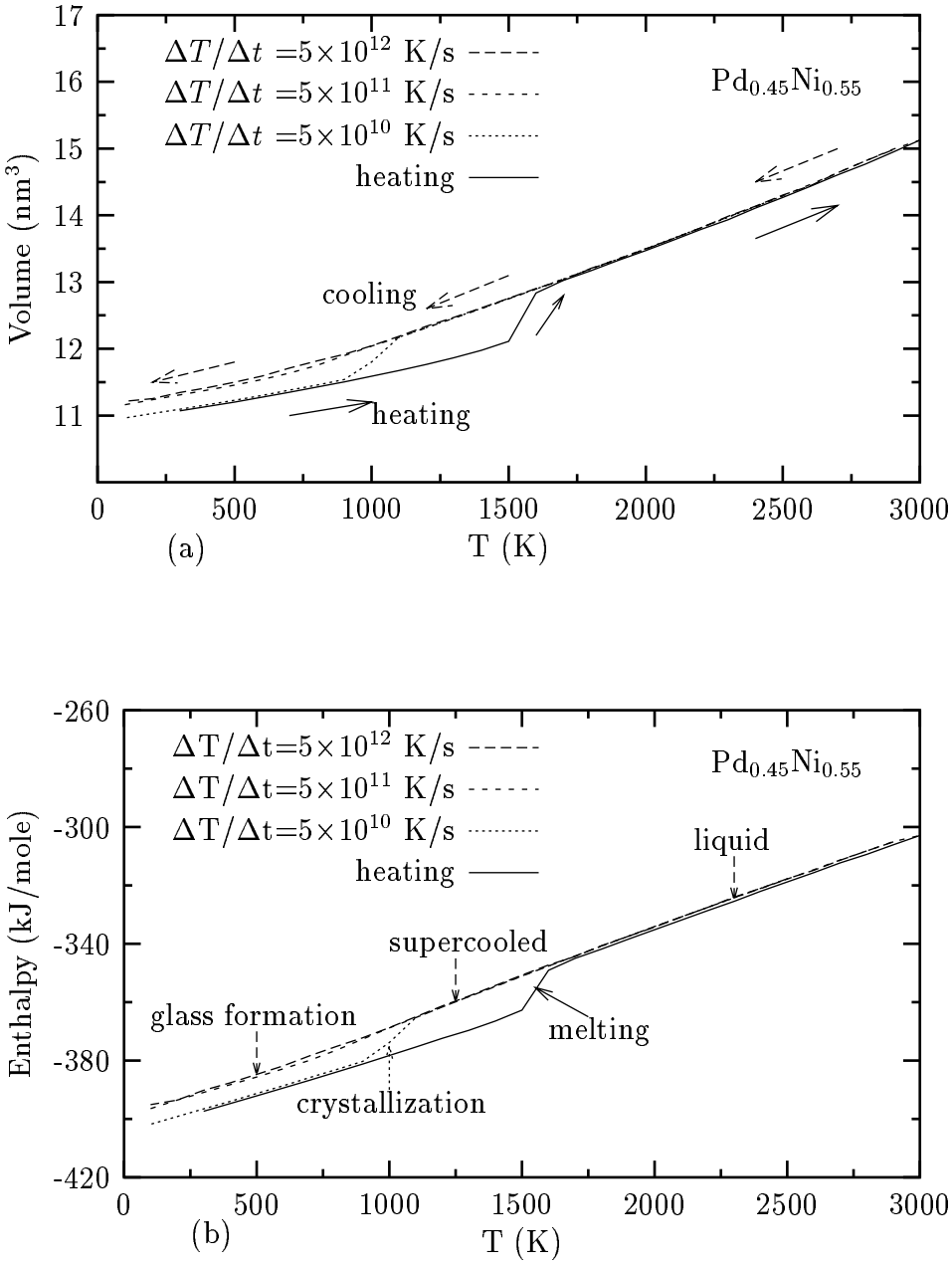

Figure 3.14: (a) The volume and (b) the enthalpy of $Pd_{0.45}Ni_{0.55}$ versus the temperature during the heating and cooling processes at the cooling rates of 5×10^{12} K/s, 5×10^{11} K/s, and 5×10^{10} K/s.

3.3.2 Pair Distribution Function

We analyze the pair distribution function, g(r), to investigate the structural properties during the heating and cooling processes. Fig. 3.15 shows g(r) of liquid, supercooled liquid and amorphous states of Pd-Ni system during fast cooling. The corresponding temperatures at each states are labeled for each curve.

The system with a random fcc crystal is heated to 3000 K and cooled back to 1900 K (above T_m). As shown in Fig. 3.15 (a), two curves of g(r) for heating and cooling processes almost overlap at the same temperature, indicating an equilibrium liquid state. Cooling to 1400 K, we still observe the structure of liquid, in fact a supercooled liquid, from Fig. 3.15 (b), while the system is in a crystalline state during the heating process. However, by further cooling to 300 K, the splitting of the second peak takes place in Fig. 3.15 (c). This splitting is known as a characteristic of metallic glasses. Hence $Pd_{0.45}Ni_{0.55}$ alloy quenched from the liquid to 300 K at the rate of 5×10^{12} K/s goes into a glassy state.

Fig. 3.16 exhibits the changes of g(r) for the Pd-Ni system during cooling process at the rate of 5×10^{10} K/s. The g(r) in the liquid and supercooled liquid phases shows the same behavior as those given in Fig. 3.15 (a) and 3.15 (b), respectively. At the temperature of 700 K, the peaks for heating and cooling processes almost overlap, forming a crystal with regular fcc structure. We can conclude from Fig. 3.16 that quenching the $Pd_{0.45}Ni_{0.55}$ alloy from the liquid to 700 K at the rate of 5×10^{10} K/s leads to crystallization.

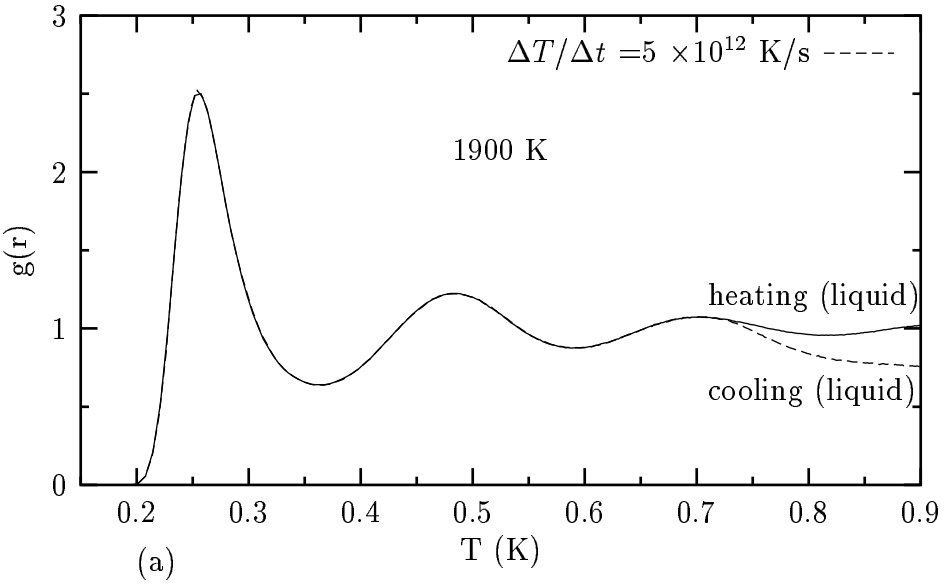

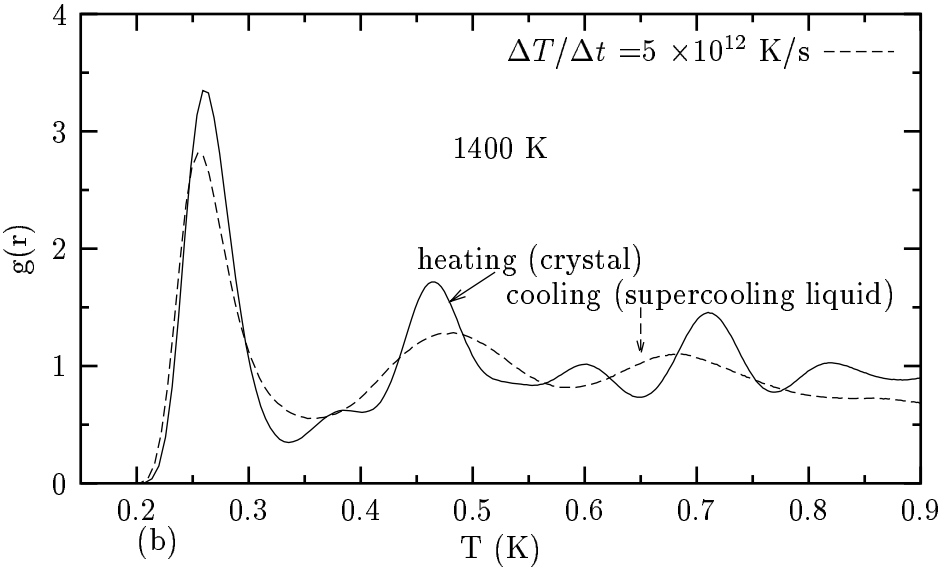

Figure 3.15: Pair distribution function g(r) of $Pd_{0.45}Ni_{0.55}$ during the heating and cooling processes at the rate of 5×10^{12} K/s. (a) At 1900 K, both structures are in liquid states. (b) At 1400 K, heating structure shows an fcc structure while cooling structure is a supercooled liquid. (c) At 300 K, heating process represents a random fcc crystal and cooling process yields a glassy phase.

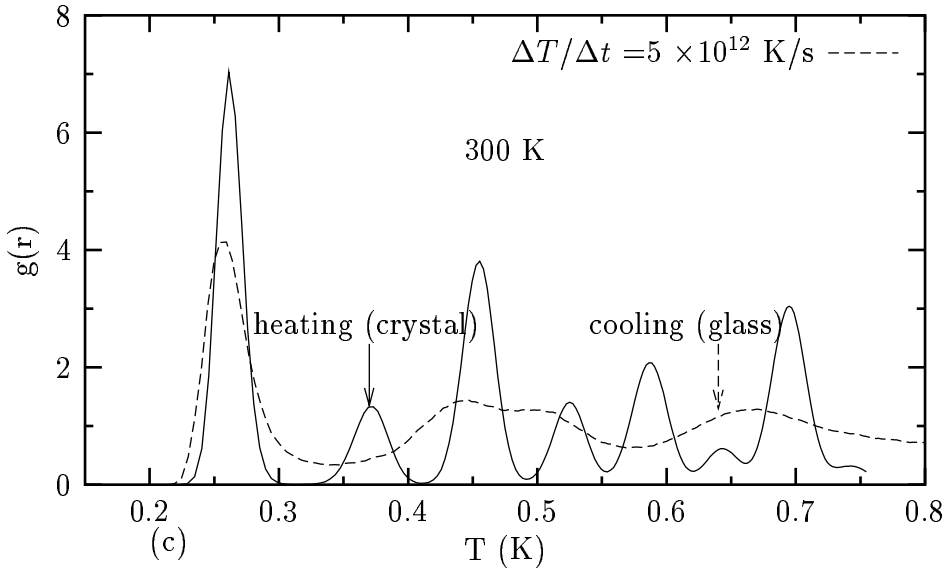

Figure 3.15: (continued).

3.3.3 Wendt-Abraham Parameter

We can determine the glass transition temperature T_g by an approach proposed by Wendt and Abraham [99]. Wendt-Abraham parameter is defined by g_{min}/g_{max}, where g_{min} and g_{max} stand for the first minimum and the maximum values of the corresponding g(r), respectively. It describes the local character of g(r) and provides a direct comparison between structures.

We quench the Pd-Ni system at several cooling rates to investigate its effect on the T_g. Fig. 3.17 (a) gives the relationship between g_{min}/g_{max} and temperature for three different cooling rates; 5×10^{12} K/s, 1×10^{12} K/s, and 5×10^{11} K/s. There exist two lines with different slopes for each cooling rate in Fig. 3.17 (a). For quantitative determination of T_g, we consider the g_{min}/g_{max} data, excluding the

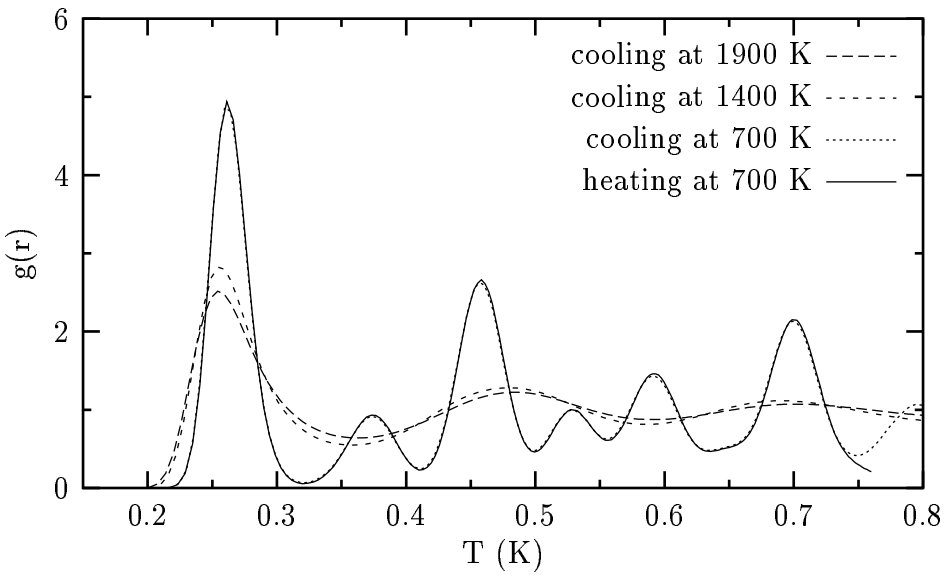

Figure 3.16: Pair distribution function g(r) of $Pd_{0.45}Ni_{0.55}$ at 700 K in the heating and the cooling processes, and at 1400 K and 1900 K in the cooling process at the rate of 5×10^{10} K/s. The system crystallizes at $\approx$ 900 K.

data close to the point where the change of slope begins. The remaining high-temperature and low-temperature data sets are fitted to linear equations with two different sets of coefficients. T_g is taken to be the temperature at which these two lines intersect each other, as shown in Fig. 3.17 (b) for the cooling rate of 5×10^{12} K/s. A similar fit is performed for volume and enthalpy versus temperature curves. This provides a nearly identical estimate of T_g. The values of T_g obtained from Wendt-Abraham parameter for various cooling rates are reported in Table 3.10. Faster cooling rates result in higher glass transition temperatures. Slower cooling rates allow a greater amount of molecular relaxation to occur in the liquid phase before the structure is frozen at the T_g, hence the glass forms at a lower temperature. The discontinuities in the constant-pressure specific

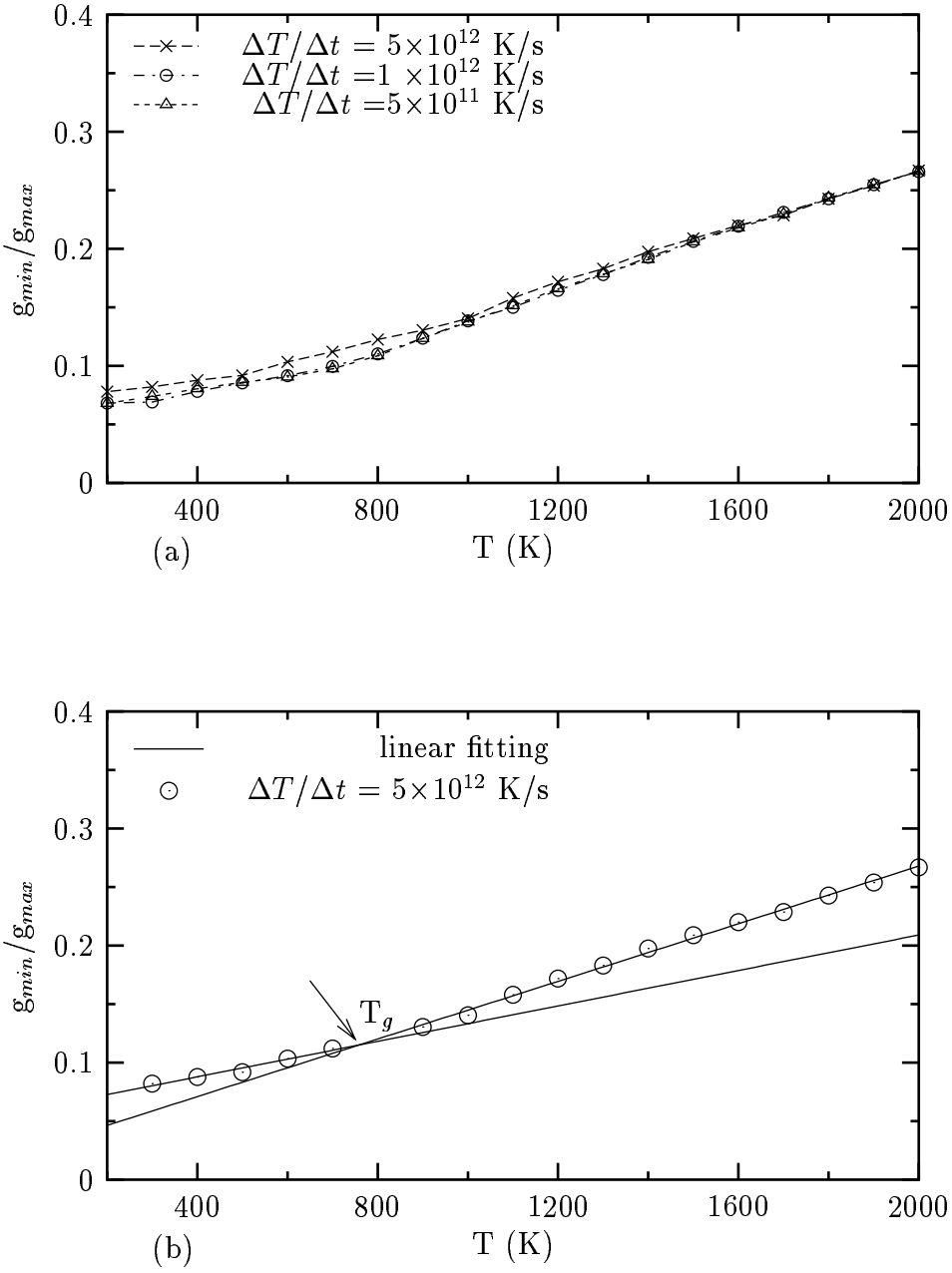

Figure 3.17: (a) Wendt-Abraham parameter (g_{min}/g_{max}) versus temperature for $Pd_{0.45}Ni_{0.55}$ obtained from three different cooling rates. (b) g_{min}/g_{max} is fitted to linear function to estimate the glass temperature T_g at the cooling rate of 5×10^{12} K/s.

heat $C_p=(\partial H/\partial T)_p$ and isobaric thermal expansion coefficient $\alpha_p=(\partial \ell nV/\partial T)_p$ in the supercooled liquid ($T_g{}^+$) and the amorphous ($T_g{}^-$) states are also given in the same table. C_p and α_p are larger in the supercooled liquid and drops to a lower value in the glassy state. As T_g decreases, C_p and α_p in the supercooled liquid increase, while those in the amorphous state decrease, depending sensitively on the value of T_g. That is, upon even slower cooling, C_p and α_p in the glassy state drop even further to lower temperatures, as discussed by Ediger *et al.* [100]. Experimental or other calculational data on T_g for $Pd_{0.45}Ni_{0.55}$ alloy are not available to compare with our results.

Table 3.10: Glass transition temperature T_g, constant-pressure specific heat C_p and thermal expansion coefficient α_p evaluated in the supercooled liquid (T_g^+) and amorphous (T_g^-) phases at $T=T_g$ for various cooling rates.

Cooling Rate ($\times 10^{12}$ K/s)	T_g (K)	$C_p(T_g^+)$ (J/mole K)	$C_p(T_g^-)$	$\alpha_p(T_g^+)$ ($\times 10^{-5}$ K^{-1})	$\alpha_p(T_g^-)$
5.0	757	33.53	29.02	11.38	7.31
1.0	670	33.67	27.38	11.45	6.69
0.5	661	33.78	26.94	11.49	6.47

3.3.4 Diffusion and Viscosity

Transport properties like diffusion and viscosity are important for understanding the dynamics of the supercooled liquid and glassy state. The diffusivity of $Pd_{0.45}Ni_{0.55}$ alloy quenched at the rate of 5×10^{11} K/s is calculated by using Einstein relation (Eq. 2.43) at TVN dynamics. The data for Pd and Ni in $Pd_{0.45}Ni_{0.55}$

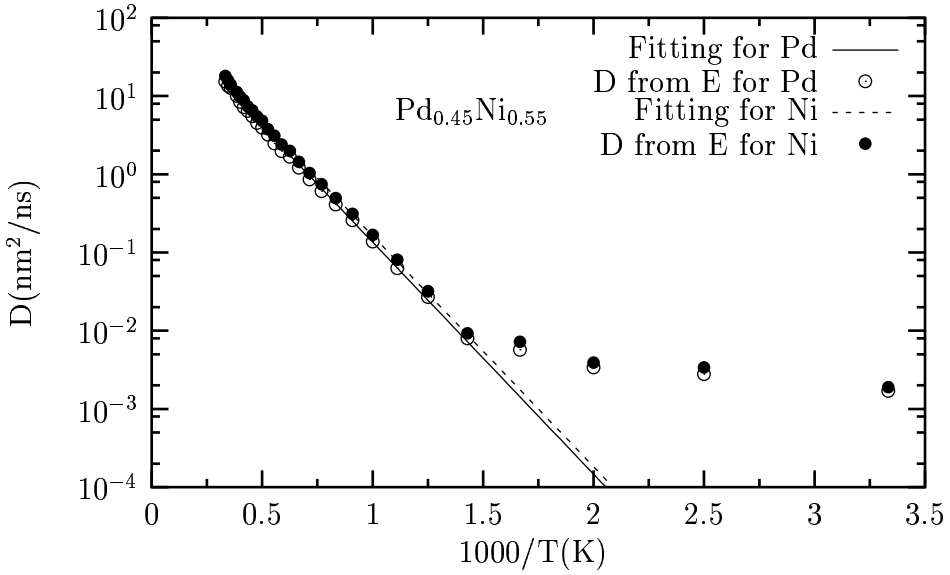

Figure 3.18: Self-diffusion coefficients D of Pd and Ni in $Pd_{0.45}Ni_{0.55}$ alloy during the cooling process at the rate of 5×10^{11} K/s. Diffusivity above the glass temperature shows the Arrhenius equation type behavior.

are reported in Fig. 3.18. Pd diffuse more slowly than the Ni despite the large advantage in the atomic size, as shown in the figure. This event can be interpreted by assuming that Pd diffuses together with cage of metal neighbors [101]. The diffusion coefficients decrease dramatically with decreasing temperature. But when the temperature reach the critical values the changes of the diffusion coefficients with temperature became small. This critical value of temperature is close to the glass transition temperature. Our result for the diffusivity above the glass transition temperature exhibits Arrhenius type temperature dependence. The discontinuity in the Arrhenius behavior near T_g is an expected result. Because the atoms lose their free volume and their only freedom is to vibrate around

their local positions as in crystalline structure. The atoms in glassy states may move by means of hopping mechanism in the system. From the plots of logD versus 1000/T, it is possible to estimate the preexponential factor D_0 and the diffusional activation energy E_a, which are 125.22 nm^2/ns and 56.77 kJ/mole for Pd, respectively, and 146.58 nm^2/ns and 56.51 kJ/mole for Ni, respectively.

The departure from the Arrhenius law in the viscosity is the most important characteristic feature of glass-forming liquids. Thus, viscosity data are used to classify glass-forming liquids according to the temperature dependence of their viscosities. Hence, we are particularly interested in viscosity at rate of 5×10^{11} K/s. The shear viscosity η is calculated from the GK relation given in Eq. 2.46 by performing MD simulations at TVN dynamics. The results for viscosity are plotted in an Arrhenius plot in which the inverse temperature axis is multiplied by the glass temperature in Fig. 3.19 (a). The viscosity increases enormously as the temperature approaches the glass transition temperature, as expected. The stress auto-correlation function (SACF) do not converge within our simulation time scale near and below the glass temperature. Hence, it is not possible to obtain viscosity data in these regions. The degree of deviation from Arrhenius behavior is called fragility and quantified by the slope m of the $\log\eta(T)$ versus T_g/T curve [102]. The fragility parameter m is about 20 for strong liquid extreme and about 200 for fragile liquid extreme [102]. We find the fragility index as 7.33 for $Pd_{0.45}Ni_{0.55}$, which indicates that Pd-Ni alloy system is a strong liquid. The strength or fragility is quantified alternatively by the strength parameter D^* in

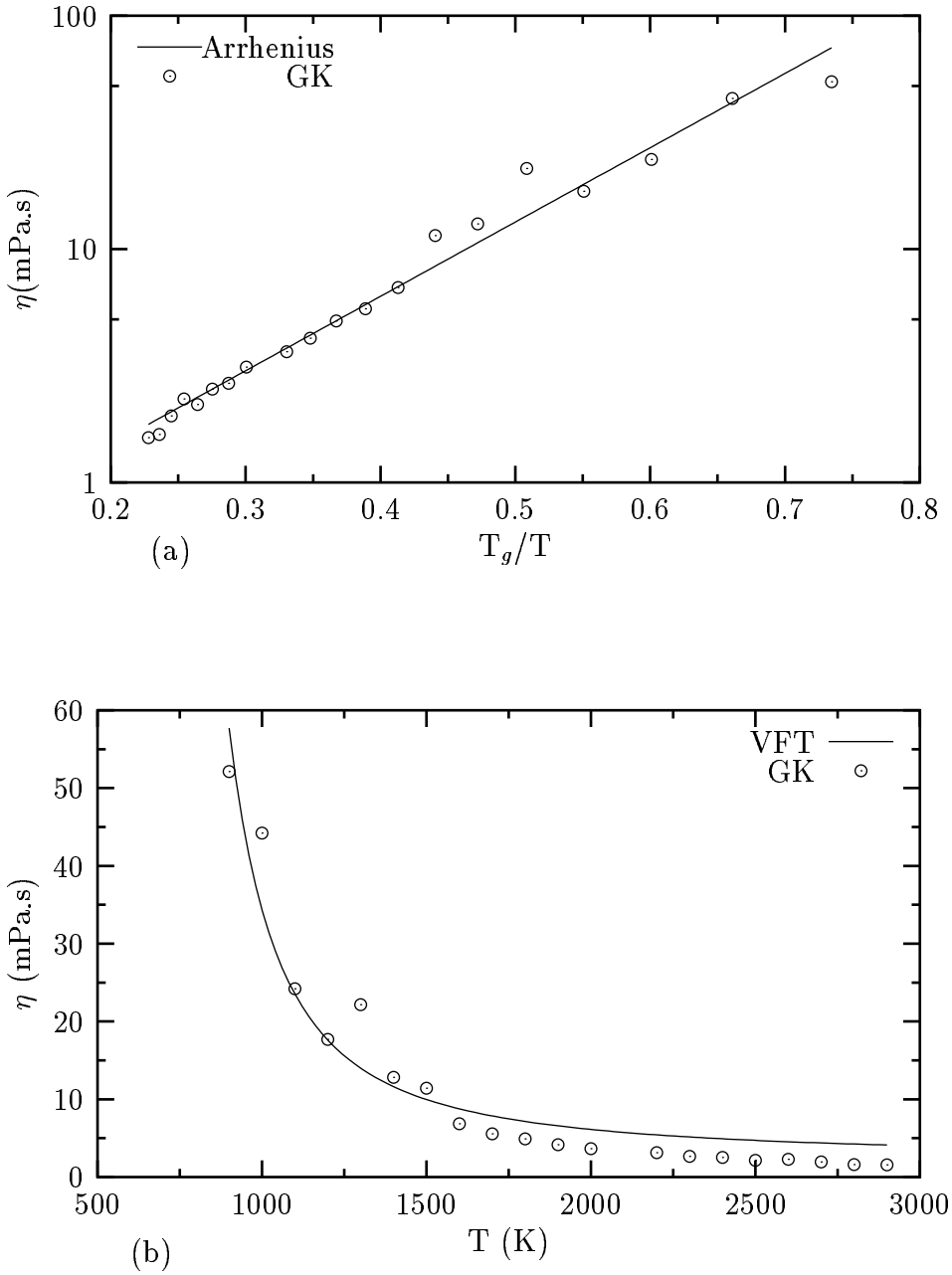

Figure 3.19: Temperature dependence of shear viscosity coefficient η for liquid and supercooled $Pd_{0.45}Ni_{0.55}$ at the rate of 5×10^{11} K/s. Circles: simulation results. Solid line: (a) Arrhenius fit and (b) fit by a Vogel-Fulcher-Tamman (VFT) relation.

the Vogel-Fulcher-Tamman (VFT) relation;

$$\eta(T) = \eta_0 exp(D^* T_0/(T - T_0)) \quad , \tag{3.3}$$

where η_0 is a constant inversely proportional to the molar volume of the liquid, and T_0 is the temperature at which the free volume is zero, being usually below T_g. Our data are fitted to the VFT equation, as shown in Fig. 3.19 (b). T_0 is taken to be 350 K. The strength parameter D^* is 5.29, allowing us to classify this binary system as a strong liquid.

CHAPTER 4

CONCLUSION

We have performed MD simulations of some static, dynamical and thermodynamical properties of disordered Pd-Ni metal alloys over a wide-range of temperatures by using Q-SC potential parameters. The SC potential parameters are also used for investigating the solid properties to see the differences between the results of two potential parameters. We have studied Pd-Ni metal alloys in three categories: solid, liquid, and glassy states. Therefore, the conclusion is given in three parts.

4.1 Solid State

The simulation results for the solid state are in agreement with the available experimental values, except for enthalpy of mixing. Our simulation results for the enthalpy of mixing show that the Pd-Ni system is immiscible in the solid phase, whereas miscible in the liquid phase, which is contrary to the experiment. The contradiction with the experiments in the enthalpy of mixing may be the shortcoming of using the potential parameters fitted to the solid state elemental properties.

The contributions up to the 8th NN shell to force constants are found sufficient to achieve convergence for the phonon dispersion calculations. Taking into

account the other N-body potentials (see Table 3.3), Q-SC potential seems to give quite an accurate description of phonon properties. Even though Q-SC potential is fitted to phonon frequencies at only the X point, the overall structure of dispersion curves are well reproduced. This potential produces better results for the transverse phonon frequencies than those obtained by pair potentials [8, 9]. We may also conclude that SC potential agrees with experimental results despite not fitting to phonon frequencies. This work also presents the phonon dispersion curves of alloys by using the SC potentials for the first time.

Elastic constants for Pd-Ni alloys, except for Pd and Ni, are also calculated by using a many body potential for the first time by this study. Homogeneous deformation and long waves methods have been used. Our results from both methods are comparable for each potential parameters. Hence the consistency condition of matching the elastic constants calculated by two methods are obtained. We have seen that Q-SC potential improves the elastic constants slightly as the temperature increases. The experimental data on the elastic constants for Pd-Ni alloys except for Pd and Ni are not available for comparison. These data may encourage the experimentalists to verify our results.

The results of solid properties show that Q-SC potential may be used to predict the lattice dynamics of fcc transition metals and their alloys with sufficient accuracy and to provide a detailed understanding of phonon properties.

The results of applicability of the Q-SC many-body potential for the properties of liquid Pd-Ni metal alloys over wide range of temperatures are presented in this study. The simulation results are compatible with the available experimental values. One of the achievements of this work is to predict the melting temperatures of Pd-Ni metal alloys with the same trend as shown by the existing experimental curve. The values of melting temperatures especially for Pd and Ni agree quite well with the experiment. The height of main S(q) peaks for Ni is found to be quite encouraging if we take into account the other simulation results in the literature.

Temperature and concentration dependence on the self diffusion coefficient D and the shear viscosity η for the Pd-Ni alloy are reported. The simulation results for these transport properties seem to exhibit Arrhenius behavior. It is also remarkable that the concentration of Ni in Pd leads to increase the diffusivity in the alloy, while it reduces the shear viscosity of the system. The experimental data on the diffusion coefficient D and shear viscosity η for Pd-Ni alloys except for Ni, are not available for comparison, but the values of D computed from Einstein and Green-Kubo relations are nearly equal to each other. The values of D for pure systems are comparable to experiment, where available, and the other simulation results, while those of η are lower. This discrepancy for viscosity can be improved by trying the non-equilibrium molecular dynamics (NEMD) technique.

Because the only experimental data for Pd-Ni metal alloys exist for the melting

points, we can test the transferability from elemental case to alloy case for melting. The results for density, static structure factor, diffusion coefficient of pure metals showing satisfactory agreement with the available experimental values lead us to conclude that transferability of the potential is proved for pure metal cases. In other words, Q-SC model is able to reproduce the thermodynamical, structural, and dynamical properties of liquid Pd, Ni, and Pd-Ni metal alloys, even though the potential parameters have been fitted solely to solid state properties of the pure system.

4.3 Glass State

We have simulated the glass formation and crystallization of bulk $Pd_{0.45}Ni_{0.55}$ metal alloy by using TPN and TVN molecular dynamics at several cooling rates. The effects of cooling rates on the physical properties, namely volume, enthalpy, pair distribution function, and Wendt-Abraham parameter are investigated. The splitting in the second peak of pair distribution function is observed during fast and intermediate cooling, indicating an amorphous state. The system goes into glassy state under quenching at the rates of 5×10^{12} K/s, 1×10^{12} K/s and 5×10^{11} K/s while it forms crystallization at the slow rate of 5×10^{10} K/s. The glass transition temperatures for different cooling rates are evaluated from volume, enthalpy and Wendt-Abraham parameter curves. We have obtained that these temperatures are nearly the same. The bigger the cooling rate, the higher the glass transition temperature.

The self-diffusion coefficients computed from TVN dynamics show Arrhenius behavior above glass temperature. The fragility parameter is calculated from viscosity data fitted to both Arrhenius and VFT relations. Viscosity data above the glass transition temperature indicate that $Pd_{0.45}Ni_{0.55}$ is strong glass former with the fragility parameter of 7.33.

In summary, the MD results reported in this study show that Q-SC model gives a good description of the thermodynamical, structural and dynamical properties of Pd-Ni metal alloys during heating and cooling processes.

The shortcoming of the simulation results for Pd-Ni metal alloy may be due to the potential parameters obtained from the physical properties of the pure metals. The simulation results may be further improved by fitting to experimental or first principle calculation of solid properties of the alloy. The concentration average may be used for combination rules for the potential parameters instead of arithmetical and geometrical average. The random initial configuration chosen by MD program may be unsuitable for simulating the system. The minimum energy configuration to start the MD calculations should be selected by using the Monte Carlo method. This may improve the simulation results better. Including the electrons to the ionic system or performing first-principle MD simulations may also improve the results further.

REFERENCES

[1] N. Singh, N. S. Banger, and S. P. Singh, Phys. Rev. **38**, 7415 (1988).

[2] G. D. Barrera and A. Batana, Phys. Rev. **47**, 8588 (1993).

[3] G. D. Barrera and A. Batana, Phys. Stat. Sol. (b) **59**, 179 (1993).

[4] N. Singh, Physica B **269**, 211 (1999).

[5] N. Singh, Phys. Rev. B **46**, 90 (1992).

[6] E. G. Brovman and Yu M. Kagan, Sov. Phys. JETP **25**, 365 (1967).

[7] W. A. Kamitakahara and B. N. Brockhouse, Phys. Rev. B **10**, 1200 (1974).

[8] S. C. Upadhyaya, J. C. Upadhyaya, and R. Shyam, Phys. Rev. B **44**, 122 (1991).

[9] C. M. I. Okeye and S. Pal, Physica B **192**, 325 (1993); Phys. Rev. B **50**, 7147 (1994).

[10] A. O. E. Animalu, Phys. Rev. B **8**, 3542 (1973); **8**, 3555 (1973).

[11] S. M. Foiles and J. B. Adams, Phys. Rev. B **40** 5909 (1989).

[12] J. Mei and J. W. Davenport, Phys. Rev. B **46**, 21 (1992).

[13] B. Sadigh and G. Grimvall, Phys. Rev. B **54**, 15742 (1996).

[14] M. M. G. Alemany, C. Rey, and L. J. Gallego, J. Chem. Phys. **109**, 3568 (1998).

[15] L. Gomez, A. Dorby, and H. T. Diep, Phys. Rev. B **55**, 6265 (1997).

[16] F. J. Cherne and M. I. Baskes, Phys. Rev. B **65**, 024209 (2001).

[17] M. I. Baskes, Phys. Rev. Lett. **83**, 2592 (1999).

[18] R. Hultgren, D. D. Desai, and D. T. Hawkins, *Selected Values of Thermodynamic Properties of Binary Alloys*, Metal Park OH:ASM (1973).

[19] P. Protopapas, H. C. Andersen, and N. A. D. Parlee, J. Chem. Phys. **59**, 15 (1973).

[20] T. Iiada and R. I. L. Guthrie, *The Physical Properties of Liquid Metals*, Clarendon Press, Oxford (1988).

[21] C. Fan, A. Takeuchi, and A. Inoue, Matter. Trans. JIM **40**, 42 (1999).

[22] P. Duwez, R. H. Willens, and W. Klement, J. Appl. Phys. **31**, 1137 (1960).

[23] A. Inoue, *Bulk Amorphous Alloys-Preparation and Fundemantel Charectiristics; Materials Science Foundations*, Vol:4, Trans. Tech., Amsterdam (1998).

[24] Z. P. Lu, Y. Li, and S. C. Ng, J. Non-Cryst. Solids **270**, 103 (2000).

[25] C. S. Liu, Z. G. Zhu, J. Xia, and D. Y. Sun J. Phys.: Condens. Matter **13**, 1873-1890 (2001).

[26] C. Kuiying, L. Hongbo, L. Xiaoping, H. Qiyong, and H. Zhuangqi, J. Phys.: Condens. Matter **7**, 2379-2394 (1995).

[27] C. S. Liu, J. Xia, Z. G. Zhu, and D. Y. Sun, J. Chem. Phys. **114**, 7506 (2001).

[28] W. Luhong, L. Hqozhe, C. Kuiying, and H. Zhuangqi, Physica B **239**, 167 (1997).

[29] K. Vollmayr, W. Kob, and K. Binder, J. Chem. Phys. **105**, 4714 (1996).

[30] F. G. Noya, C. Rey, and L. J. Gallego, J. Non-Cryst. Solids **298**, 60 (2002).

[31] Y. Qi, T. Çağın, Y. Kimura, and W. A. Goddard III, Phys. Rev. B **59**, 3527 (1999).

[32] M. Uludoğan, Ph. D. Thesis, METU Univ., Ankara, Turkey (2003).

[33] R. Car and M. Parrinello, Phys. Rev. Lett. **55**, 2471 (1985).

[34] J. K. Norskov, Phys. Rev. B **26**, 2875 (1982).

[35] M. S. Daw and M. I. Baskes, Phys. Rev. B **29**, 6443 (1984).

[36] M. W. Finnis and J. E. Sinclair, Phil. Mag. A **50**, 45 (1984).

[37] A. P. Sutton and J. Chen, Phil. Mag. Lett. **61**, 139 (1990).

[38] R. M. Lyndenbell, Surf. Sci. **259**, 129 (1991).

[39] J. Uppenbrink, D. J. Wales, A. I. Kirkland, D. A. Jefferson and J. Urban, Philos. Mag. B **65**, 1079 (1992).

[40] K. D. Hammonds and R. M. Lyndenbell, Surf. Sci. **278**, 437 (1992).

[41] B. D. Todd and R. M. Lyndenbell, Surf. Sci. **328**, 170 (1995).

[42] D. J. Wales and L. J. Munro, J. Phys. Chem. **100**, 2053 (1996).

[43] G. Dereli, T. Çağın, M. Uludoğan, and M. Tomak, Philos. Mag. Lett. **75**, 209 (1997).

[44] T. Çağın, G. Dereli, M. Uludoğan, and M. Tomak, Phys. Rev. B **59**, 3468 (1999).

[45] T. Çağın, Y. Qi, H. Li, Y. Kimura, H. Ikeda, W. L. Johnson, and W. A. Goddard III, MRS Symp. Ser. **554**, 43 (1999).

[46] H. Ikeda, Y. Qi, T. Çağın, K. Samwer, W. L. Johnson, and W. A. Goddard III, Phys. Rev. Lett. **82**, 822900 (1999).

[47] Y. Qi, T. Çağın, W. L. Johnson, and W. A. Goddard III, J. Chem. Phys. **115**, 385 (2001).

[48] A. Strachan, T. Çağın, and W.A. Goddard III, Phys. Rev. B **63**, 0601103 (2001).

[49] Y. Qi, T. Çağın, Y. Kimura, and W. A. Goddard III, J. Comp. Aid. Mat. Des. **8**, 233 (2002).

[50] S. Özdemir Kart, M. Tomak, and T. Çağın, *Phonon Dispersions and Elastic Constants of Disordered Pd-Ni Alloys*, submitted (2004).

[51] S. Özdemir Kart, M. Tomak, M. Uludoğan, and T. Çağın, *Liquid Properties of Pd-Ni Alloys*, J.Non-Cryst. Solids, in press (2004).

[52] S. Özdemir Kart, M. Uludoğan, M. Tomak, and T. Çağın, *Solid and Liquid Properties of Pd-Ni Metal Alloys Using Quantum Sutton-Chen Many-Body Potential*, in press at Nanoenginered Nanofibrous Materials, Nato Science Series by S. Güceri, Y. Gogotsi and W. Kuzentsov, Kluwer Academic Book Publishers, Netherlands (2004).

[53] D. Frenkel and B. Smit, *Understanding Molecular Simulation from Algorithms to Applications*, Academic Press, San Diego (1996).

[54] M. P. Allen and D. J. Tildesley, *Computer Simulation of Liquids*, Oxford Science Publications, New York (1987).

[55] J. P. Hansen and I. R. McDonald, *Theory of Simple Liquids*, Academic Press, London (1986).

[56] J. M. Haile, *Molecular Dynamics Simulation*, Wiley & Sons Publication, Canada (1992).

[57] A. R. Leach, *Molecular Modelling Principles and Applications*, Longman, Edinburg (1996).

[58] H. C. Andersen, J. Chem. Phys. **72**, 2384 (1980).

[59] M. Parrinello and A. Rahman, Phys. Rev. Lett. **45**, 1196 (1980).

[60] S. Nosé, J. Chem. Phys. **81**, 511 (1984).

[61] W. G. Hoover, Phys. Rev. A **31**, 1695 (1985).

[62] J. R. Ray and A. Rahman, J. Chem. Phys. **82**, 4243 (1985).

[63] H. Rafii-Tabar, Phys. Rep. **325**, 239 (2000); **365**, 145 (2002).

[64] C. W. Gear, *Numerical Initial Value Problems in Ordinary Differential Equations*, Prentice-Hall, NJ (1971).

[65] K. Maeda, V. Vitek, and A. P. Sutton, Acta Metall. **30**, 2001 (1982).

[66] F. Ercolessi, M. Parinello, and F. Tosatti, Phil. Mag. A **58**, 213 (1988).

[67] M. J. Stott and E. Zaremba, Phys. Rev. B **22**, 1564 (1980).

[68] J. K. Norskov and N. O. Lang, Phys. Rev. B **21**, 2131 (1980).

[69] G. J. Ackland, G. Tichy, V. Vitek, and M. W. Finnis, Phil. Mag. A **56**, 735 (1987).

[70] K. Masuda and A. Sato, Phil. Mag. A **44**, 799 (1981).

[71] H. Rafii-Tabar and A. P. Sutton, Philos. Mag. Lett. **63**, 217 (1991).

[72] T. Çağın and J. R. Ray, Phys. Rev. A 37, 247 (1988); Phys. Rev. B **37**, 699 (1988); Phys. Rev. B **38**, 7940 (1988).

[73] A. A. Maradudin, E. W. Montroll, and G. H. Weiss, *Theory of Lattice Dynamics in the Harmonic Approximation*, Academic Press (1971).

[74] P. Bruesch, *Phonons: Theory and Experiments I. Lattice Dynamics and Models of Interatomic Forces*, Springer-Verlag, New York (1982).

[75] M. T. Dove, *Introduction to Lattice Dynamics*, Cambridge University Press, New York (1993).

[76] E. Rabani, J. D. Gezelter, and B. J. Berne, J. Chem. Phys. **107**, 6867 (1997).

[77] G. J. Ackland and V. Vitek, Phys Rev B **41**, 10324 (1990).

[78] C. Kittel, *Introduction to Solid State Physics*, Wiley, New York (1996).

[79] A. P. Miller and B. N. Brockhouse, Can. J. Phys. **49**, 704 (1971).

[80] R. J. Birgeneau, J. Cords, G. Dolling, and A. D. W. Woods, Phys. Rev. **136**, A1359 (1964).

[81] Landolt-Bornstein, *Zahlenwerte und Funktionen aus Naturwisso und Technik*, New Series III-13 a, Springer-Verlag, Berlin (1981).

[82] F. Cleri and V. Rosato, Phys. Rev. B **48**, 22 (1993).

[83] G. Simmons and H. Wang, *Single Crystal Elastic Constant and Calculated Aggregate Properties*, MIT Press, Cambridge (1971).

[84] S. M. Foiles, M. I. Baskes, and M. S. Daw, Phys. Rev. B **33**, 7983 (1986).

[85] M. J. Mehl and D. A. Papaconstantopolos, Phys. Rev. B **54**, 4519 (1996).

[86] Y. Waseda, *The Structure of Non-Crystalline Materials-Liquid and Amorphous Solids*, Mc Graw Hill, New York (1980).

[87] S. M. Foiles, Phys. Rev. B **32**, 3409 (1985).

[88] L. M. Holzman, J. B. Adams, S. M. Foiles, and W. N. G. Hitchan, J. Mater. Res. **6**, 298 (1991).

[89] M. M. G. Alemany, C. Rey, and L. J. Gallego, Phys. Rev. B **58**, 685 (1998).

[90] M. M. G. Alemany, O. Dieguez, C. Rey, and L. J. Gallego, Phys. Rev. B **60**, 9208 (1999).

[91] M. Khetarpal, D. Bhandari, and N. S. Saxena, Physica B **254**, 52 (1998).

[92] I. Yokoyama, Physica B **271**, 230 (1999).

[93] J. Mei and J. W. Davenport, Phys. Rev. B **42**, 9682 (1990).

[94] M. M. G. Alemany, C. Rey, and L. J. Gallego, J. Chem. Phys. **109**, 5175 (1998).

[95] I. Egry, Scr. Metall. Mater. **28**, 1273 (1993).

[96] I. Yokoyama and T. Arai, J. Non-Cryst. Solids **293-295**, 806 (2001).

[97] F. J. Cherne, M. I. Baskes, and B. L. Holian, Phys. Rev. B **67**, 092104 (2003).

[98] F. F. Abraham, J. Chem. Phys. **72**, 359 (1980).

[99] H. R. Wendt and F. F. Abraham, Phys. Rev. Lett. **41**, 1244 (1978).

[100] M. D. Ediger, C. A. Angell, and S. R. Nagel, J. Phys. Chem. **100**, 13200 (1996).

[101] P. Ballone and S. Rubini, Phys. Rev. B **51**, 14962 (1995).

[102] R. Böhmer, K. L. Ngai, C. A. Angell, and D. J. Plazek, J. Chem. Phys. **99**, 4201 (1993).

VITA

Sevgi Özdemir Kart was born in 1970 in Ankara. She recieved her B.S. degree in Physics in 1993 at Middle East Technical University. She acquired her M.S. degree in Condensed Matter in 1997 at METU. Her master thesis title is *Identification of Several Energy Transfer Pathways in the Light-Harvesting Complex II of Plants Using Current Structural and Spectroscopic Information.* Presently, she works as a research assistant in the Physics Department, METU, Ankara.